Research Paper

GEOSPHERE

GEOSPHERE

https://doi.org/10.1130/GES02619.1

16 figures; 2 tables; 1 set of supplemental files

CORRESPONDENCE: azuza@unr.edu

CITATION: Zuza, A.V., and Dee, S., 2023, Decoupled Oligocene mylonitic shearing and Miocene detachment faulting in the East Humboldt Range metamorphic core complex, northeast Nevada, USA: Geosphere, https://doi.org/10.1130/GES02619.1.

Science Editor: Christopher J. Spencer
Associate Editor: Jason W. Ricketts

Received 21 October 2022
Revision received 13 April 2023
Accepted 22 May 2023

Published online 20 July 2023

Decoupled Oligocene mylonitic shearing and Miocene detachment faulting in the East Humboldt Range metamorphic core complex, northeast Nevada, USA

Andrew V. Zuza and Seth Dee

Nevada Bureau of Mines and Geology, University of Nevada, Reno, Nevada 89557, USA

ABSTRACT

The relationships between brittle detachment faulting and ductile shear zones in metamorphic core complexes are often ambiguous. Although it is commonly assumed that these two structures are kinematically linked and genetically related, direct observations of this coupling are rare. Here, we conducted a detailed field investigation to probe the connection between a detachment fault and mylonitic shear zone in the Ruby Mountain–East Humboldt Range metamorphic core complex, northeast Nevada. Field observations, along with new and published geochronology, demonstrate that Oligocene top-to-the-west mylonitic shear zones are crosscut by ca. 17 Ma subvertical basalt dikes, and these dikes are in turn truncated by middle Miocene detachment faults. The detachment faults appear to focus in preexisting weak zones in shaley strata and Mesozoic thrust faults. We interpret that the Oligocene mylonitic shear zones were generated in response to domal upwelling during voluminous plutonism and partial melting, which significantly predated the middle Miocene onset of regional extension and detachment slip. Our model simplifies mechanical issues with low-angle detachment faulting because there was an initial dip to the weak zones exploited by the future detachment-fault zone. This mechanism may be important for many apparent low-angle normal faults in the eastern Great Basin. We suggest that the temporal decoupling of mylonitic shearing and detachment faulting may be significant and underappreciated for many of the metamorphic core complexes in the North American Cordillera. In this case, earlier Eocene–Oligocene buoyant doming may have preconditioned the crust to be reactivated by Miocene extension, thus explaining the spatial relationship between structures.

INTRODUCTION

Continental metamorphic core complexes in the North American Cordillera involve deep (mid- to lower crust) rocks juxtaposed against brittle highly extended upper-plate rocks (e.g., Armstrong, 1972; Coney, 1974; Crittenden et al., 1980; Lister and Davis, 1989). This configuration is generally attributed to regional extension with large displacement accommodated along low-angle brittle normal faults that link downdip with ductile shear zones (e.g., Davis et al., 1986; Lister and Davis, 1989; Spencer and Reynolds, 1989; Wernicke et al., 1992; Platt et al., 2015). However, the extent to which brittle detachment faulting is temporally coupled and genetically related to exhumed ductile shear zones is usually hard to confirm. For example, Ducea et al. (2020) recently argued that mylonitic, ductile fabrics in the Catalina metamorphic core complex of southern Arizona formed during Eocene magmatism, well before Oligocene–Miocene regional extension, although this interpretation has been disputed (e.g., Spencer et al., 2022). Similarly, there is growing evidence that Miocene detachment faults in southern California and Arizona are exhuming footwall rocks that at least partially consist of older Late Cretaceous-Paleogene Laramide-aged shear zones (e.g., Bykerk-Kauffman and Janecke, 1987; Jaramillo et al., 2022; Wong et al., 2023). Mylonitic fabrics of the metamorphic core complexes in Nevada and Utah are interpreted to have formed primarily in the Paleogene (Wright and Snoke, 1993; Konstantinou et al., 2013; Lee et al., 2017; Zuza et al., 2022a) prior to the initiation of regional Miocene extension (Miller et al., 1999; Colgan and Henry, 2009; Zuza and Cao, 2023). Conversely, some refined models of metamorphic core complex development in the Colorado River extensional corridor emphasize that they may consist of Miocene brittle detachment faults capturing and exhuming kinematically similar subhorizontal ductile shear zones (e.g., Davis, 1988; Singleton and Mosher, 2012).

This problem is particularly enigmatic because absolute timing constraints at the needed resolution to differentiate or correlate brittle and ductile phases of deformation are commonly lacking. Because these phases of deformation may, or may not, be temporally and spatially coupled, we refer to the main phases of metamorphic core complex development as those that resulted in mylonitic shearing, significant lower-plate exhumation, and possibly synkinematic partial melting. Although many models for metamorphic core complex generation link brittle (commonly low-angle) large-displacement detachment slip with mylonitic shearing, here we avoid assuming this genetic relationship without supporting evidence. To address some of these issues, this study focused on exploring the relationship between low-angle

Andrew V. Zuza https://orcid.org/0000-0001-6130-5121

detachment faulting and mylonitic shearing in the Ruby Mountains–East Humboldt Range metamorphic core complex of northeast Nevada (Fig. 1). This metamorphic core complex has been studied in great detail over the past several decades (e.g., Howard, 1980; Snoke, 1980; McGrew et al., 2000; Colgan et al., 2010), but there has not yet been a modern synthesis and kinematic model to describe Cenozoic deformation, including the relative roles of ductile shearing versus brittle faulting. In a previous study, we analyzed the ductilely deformed, mylonitized lower plate of the Ruby Mountains–East Humboldt Range, including kinematic analysis, microstructural observations, U-Pb zircon dating, and isotopic characterization to reveal significant structural attenuation that occurred in the Oligocene (Zuza et al., 2022a). Here, in this present work, we present new detailed geologic mapping in the East Humboldt Range, structural analysis, and U-Pb zircon dating that constrain the structural evolution of upper-plate detachment faulting, which places unmetamorphosed Upper Paleozoic strata over the mylonitic lower plate. Furthermore, our constraints from field relationships unequivocally show that Miocene low-angle detachment faulting was temporally decoupled from Oligocene mylonitic shearing. The main phase of metamorphic core complex development, with synkinematic partial melting and ductile attenuation, occurred in the Oligocene, whereas Miocene detachment faulting was related to regional Basin and Range extension.

Based on updated field relationships, we present a complete kinematic model of Cenozoic deformation that includes Oligocene doming and ductile shearing subsequently reactivated by Miocene detachment faulting. This reconstruction shows that the primary Ruby Mountain–East Humboldt Range detachment fault was generated in heterogeneous, moderately dipping (~>40°) layers, which simplifies issues of the mechanical feasibility of low-angle normal faults (e.g., Axen, 2004; Collettini, 2011). Insights from the Ruby Mountains–East Humboldt Range are likely applicable to other metamorphic core complexes in the North American Cordillera, especially those in Nevada and Utah (Fig. 1).

GEOLOGIC BACKGROUND

The East Humboldt Range is the northern extent of the coupled Ruby Mountains–East Humboldt Range metamorphic core complex system (Fig. 1). The range exposes a mylonitized and attenuated lower plate consisting of metamorphosed Proterozoic–Paleozoic paragneiss and deformed Mesozoic–Cenozoic igneous rocks, an upper plate consisting of Upper Paleozoic rocks that are faulted but not penetratively strained, and faulted and tilted Miocene volcanic rocks with interbedded sedimentary strata (Figs. 1–3; Howard, 1980; Snoke, 1980; Snoke and Miller, 1988; Snoke et al., 1990, 1997; McGrew et al., 2000; Colgan et al., 2010; Henry et al., 2011; Howard et al., 2011; Lund Snee et al., 2016). Zuza et al. (2022a) previously provided an overview of the mylonitic bedrock units that make up the lower plate of the core complex, and in this work, we mostly focus on the upper-plate structures and stratigraphy.

The Proterozoic–middle Paleozoic paragneiss bedrock experienced a poorly constrained phase of Jurassic and Cretaceous contractional deformation, including the generation and intrusion of voluminous Late Cretaceous leucogranite (Hudec, 1992; Jones, 1999; McGrew et al., 2000; Lee et al., 2003; Howard et al., 2011; Hallett and Spear, 2014, 2015). These rocks were intruded by Eocene and Oligocene intrusions and sheared and attenuated with top-to-the-W kinematics (Snoke, 1980; Dokka et al., 1986; Hurlow et al., 1991). The most significant phase of mylonitic shearing occurred during the Oligocene (e.g., Wright and Snoke, 1993; Zuza et al., 2022a), although pre-Oligocene deformation may have occurred but was overprinted. Specifically, there was likely Jurassic–Cretaceous contractional deformation, and there was possibly an early Eocene phase of deformation as tracked via thermochronology and petrochronology (McGrew and Snee, 1994; McGrew et al., 2000; Hallett and Spear, 2015). Evidence for a major phase of Oligocene shearing includes (1) deformation of large-volume Oligocene (ca. 31–29 Ma) monzogranite plutons in the East Humboldt Range with parallel kinematics and lineations to the rest of the mylonites in the range (e.g., Wright and Snoke, 1993; Zuza et al., 2022a); (2) ca. 25–22 Ma muscovite and biotite $^{40}Ar/^{39}Ar$ dates and overlapping titanite, apatite, and zircon fission-track ages from samples across the East Humboldt Range and Ruby Mountains (Dallmeyer et al., 1986; Dokka et al., 1986; McGrew and Snee, 1994; Gifford et al., 2008) that suggest cooling below the nominal temperatures of quartz plasticity (i.e., below 300 °C, which is also approximately the closure temperature of Ar diffusion in biotite; Harrison et al., 1985); (3) poorly dated, but probably late Oligocene syn- and postkinematic leucogranite dikes that crosscut mylonitic fabrics (e.g., Zuza et al., 2022a), and (4) undeformed ca. 17 Ma basalt dikes with chilled margins that crosscut mylonitic fabrics (Table 1; Snoke, 1980; Zuza et al., 2021b; this study). Mylonitic shearing appears to be restricted to rocks at and below the Mississippian Diamond Peak Formation and Chainman Shale (Figs. 3C and 4). It is possible that higher mylonitic shearing was excised or obscured via later detachment faulting.

Unmetamorphosed Upper Paleozoic rocks, including the Mississippian Diamond Peak Formation to Permian strata, are faulted onto the mylonite zone along a brittle, low-angle detachment fault known regionally as the Ruby Mountain–East Humboldt Range detachment fault (e.g., Dokka et al., 1986; Hurlow, 1987; Snoke et al., 1990; Haines and van der Pluijm, 2010). These upper-plate rocks are exposed north and south of the Secret Creek gorge (Fig. 1), in geologic maps of the Secret Valley, Soldier Peak, and Tent Mountain quadrangles (Snoke, 1980; Snoke et al., 2021, 2022; Zuza et al., 2021a). This relationship was investigated in more detail in this present study.

Along the northeastern flank of the East Humboldt Range, Cenozoic volcanic and sedimentary deposits overlie Middle–Upper Paleozoic rocks, which are together high-angle normal faulted against metamorphosed lower-plate rocks (Figs. 1 and 2; McGrew and Snoke, 2015; McGrew, 2018). Prior published mapping around Clover Creek and Clover Hill east of the East Humboldt Range (McGrew and Snoke, 2015; McGrew, 2018) and our updated field observations show that the sequence of Upper Paleozoic rocks and the Cenozoic deposits are located within a graben bounded by inward-dipping moderate-to-high-angle normal faults

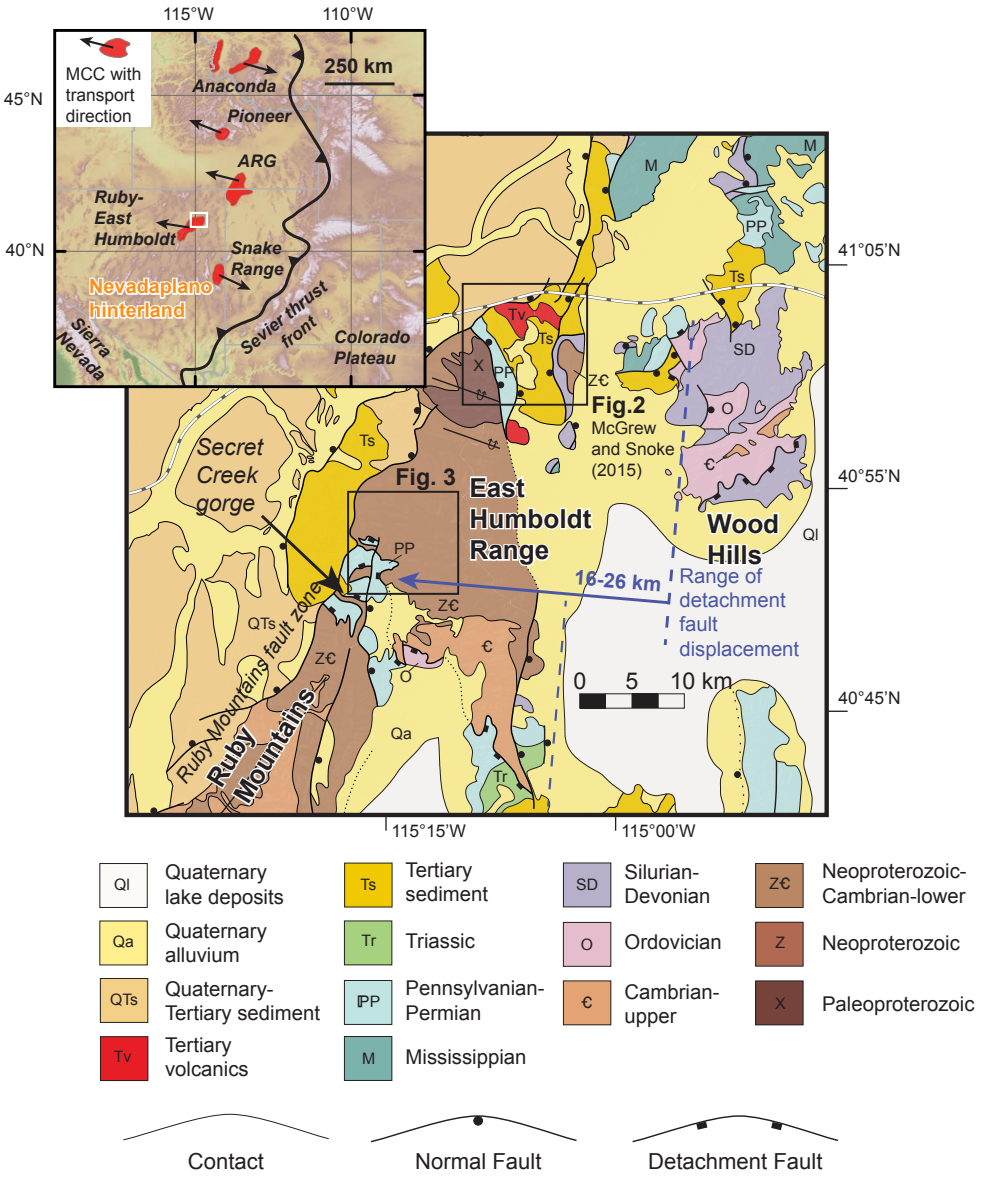

Figure 1. Geologic map of the study area in northeast Nevada, from the East Humboldt Range in the west to the Wood Hills in the east, modified from Zuza et al. (2022a), adapted from Coats (1987) and Zuza et al. (2021b). Note the location of the geologic maps in Figure 2 (McGrew and Snoke, 2015) and Figure 3 (this study). Blue displacement vector and estimates are discussed in the text. Top-left inset shows study area (white box) within the context of the Great Basin and other nearby metamorphic core complexes (MCC). ARG—Albion–Raft River–Grouse Creek metamorphic core complex.

(Fig. 2). The Upper Paleozoic rocks and the Cenozoic deposits are in detachment-fault contact above the metamorphosed, mylonitic rocks, as observed around Clover Hill (Fig. 2; McGrew and Snoke, 2015). This detachment is mostly not exposed in the Clover Creek and Willow Creek lowlands because of high-angle normal faults that dropped the detachment to a structurally lower position in the subsurface. However, this detachment-fault system is probably part of the same overall system exposed around Secret Creek gorge (Fig. 1) as either the same fault or a related splay. Specifically, east-tilted Tertiary volcanic rocks in the Clover Creek valley are truncated by a detachment fault above mylonitic Paleozoic–Proterozoic strata, with an ~45° cutoff relationship (Fig. 2). These relationships suggest that the breakaway of this detachment-fault system must be located to the east, where the Tertiary hanging-wall rocks restore to, possibly above the Wood Hills or Pequop Mountains (e.g., Camilleri and Chamberlain, 1997; Zuza et al., 2021b). For example, in the Wood Hills, a package of Tertiary deposits similar to the Clover Creek sequence, including Eocene tuff and Miocene sedimentary rocks, is faulted over Middle Paleozoic rocks (Fig. 1; e.g., Brooks et al., 1995; Camilleri, 2010b).

Existing evidence suggests that much of this detachment-fault history occurred in the middle–late Miocene (Table 1). The detachment fault crosscuts a ca. 17 Ma basalt dike in the Dorsey Creek drainage, just north of the Secret Creek gorge (Snoke, 1980; this study). Furthermore, there is indirect evidence for detachment faulting from inferences of significant middle–late Miocene exhumation based on the basin record (discussed in the next paragraphs) and apatite fission-track and (U-Th)/He thermochronology traverses of Colgan et al. (2010) that show rapid cooling at ca. 17–15 Ma (Table 1).

The Cenozoic extensional history is recorded in Cenozoic basins in northeast Nevada, including the Eocene Elko and Copper, Oligocene(?)–Miocene Clover Creek, and Miocene Humboldt basins (Henry, 2008; Henry et al., 2012; McGrew and Snoke, 2015; Smith et al., 2017; Canada et al., 2019; Zuza et al., 2021b). The Eocene Elko basin is widely

distributed west of the East Humboldt Range, but the comprising sediments are generally thin (<1 km), consisting of ca. 48–38 Ma lacustrine and volcaniclastic sediment deposits (e.g., Solomon et al., 1979; Haynes, 2003; Lund-Snee et al., 2016; Smith et al., 2017). The distribution of thickness of Eocene deposits (Smith et al., 2017) suggests they filled in paleovalleys incised in a thickened hinterland plateau (Henry, 2018). Minor-displacement normal faults appear to have been active coeval with the Eocene basin, although there is no evidence for widespread extension or significant relief generation.

The existence of any potential Oligocene basin is particularly enigmatic but important given the interpretation of Oligocene mylonitic shearing in the East Humboldt Range. The only reported possible case for Oligocene basin sedimentation is an ~3-km-thick Clover Creek sedimentary section in the East Humboldt Range that contains Eocene through Middle Miocene deposits (Fig. 2; Snelson, 1957; McGrew and Snoke, 2015; Zuza et al., 2021b). Zuza et al. (2021b) recently provided an overview and updated geochronology from this stratigraphic section. Their updated dating suggests <500 m of section could have a late Oligocene–early Miocene age, but this section lacks absolute age constraints and could also be middle Miocene in age.

Miocene basin deposits are widespread across northeast Nevada and are collectively part of the

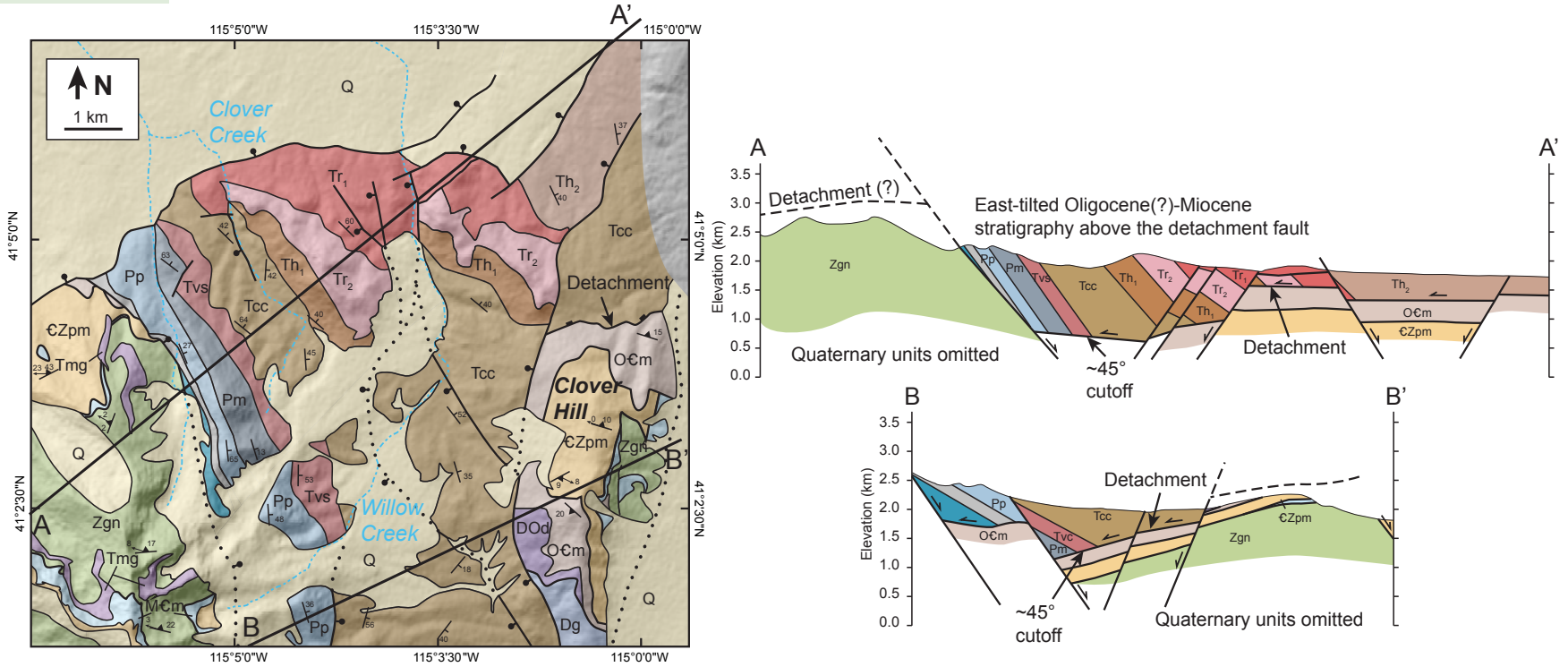

Figure 2. Simplified geologic map of the northeastern flank of the East Humboldt Range, adapted from the 1:24,000 scale geologic map of McGrew and Snoke (2015) with minimal modifications by the authors of this present study based on new geologic mapping. Cross-sections A-A′ and B-B′ were redrafted based on the original style and relationships of McGrew and Snoke (2015), with minor modifications to better reflect our interpretations of the map relationships.

(A)

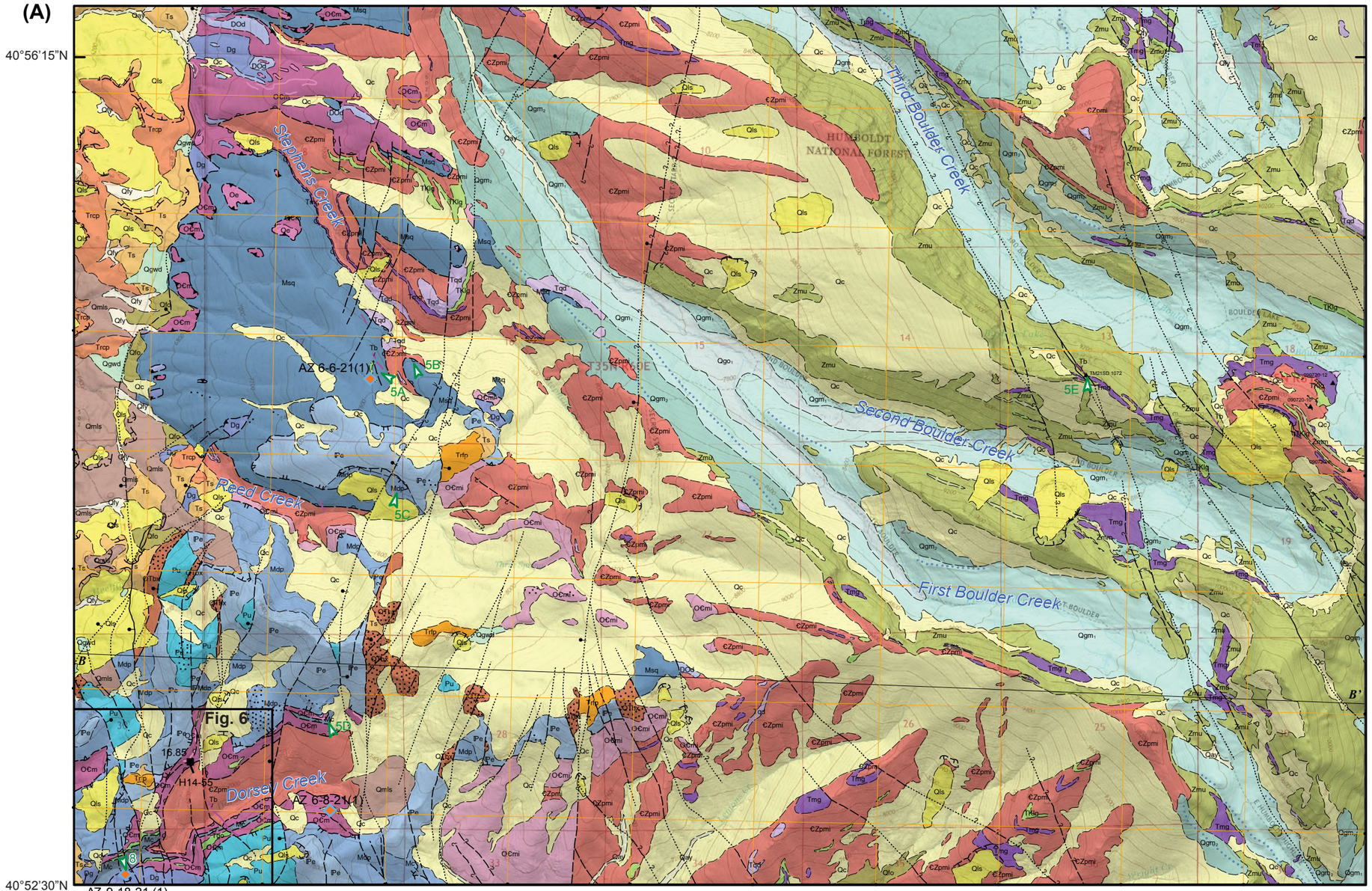

Figure 3. (A) Geologic map of the southern Tent Mountain quadrangle (Zuza et al., 2021a) at ~1:48,000 scale, with attitudes removed for clarity. Stereonet plot shows poles-to-planes of subhorizontal bedding and foliation, with northwest-trending lineations. (B) Unit explanation for the geologic map. (C) Geologic cross section across B-B'. (***Continued on following page.***)

Contact Solid where certain, dashed where approximately located.

Fault Dashed where approximately located, dotted where concealed; queried if identity or existence uncertain.

Normal fault Dashed where approximately located, dotted where concealed; queried if identity or existence uncertain.

Low-angle fault Dashed where approximately located. Semicircles on upper plate.

Detachment fault Dashed where approximately located, dotted where concealed. Hachures on upper plate.

Thrust fault Dashed where approximately located, queried if identity or existence uncertain. Sawteeth on upper plate.

Landslide scarp Solid where certain. Hachures downscarp.

Glacial moraine crests

Silica alteration

Analytical samples

AZ7-28-20(4) U-Pb zircon

16.85 H14-55 $^{40}Ar/^{39}Ar$ (age, Ma)

5A Field photo and view direction (number is figure, letter is panel)

0 0.5 1 km (~1:48,000 scale)

Lower plate

- Foliations (n=1510)
- Lineations (n=1146)

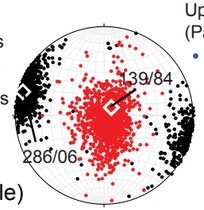

Upper plate (Paleozoic strata)

- Bedding (n=218)

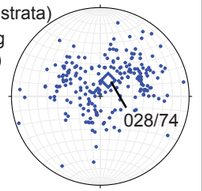

(B) Geologic Units

QUATERNARY DEPOSITS

- Qc — Colluvium (Holocene)
- Qls — Landslide deposits (Holocene to Pleistocene)
- Qlsm — Slide block of marble in landslide deposit (Holocene to Pleistocene)
- Qay — Active alluvium (Holocene)
- Qfy_1 — Youngest alluvial-fan deposits (late Holocene)
- Qfy_2 — Young alluvial-fan deposits (middle to early Holocene)
- Qfy — Young alluvial-fan deposits, undivided (Holocene)
- Qfi — Intermediate-aged alluvial-fan deposits (late Pleistocene)
- Qgo_1 — Glacial outwash deposits (late Pleistocene)
- Qgm_1 — Glacial moraine deposits (late Pleistocene)
- Qgo_2 — Glacial outwash deposits (middle Pleistocene)
- Qgm_2 — Glacial moraine deposits (middle Pleistocene)
- Qgwd — Groundwater discharge deposits (Holocene to Pleistocene)
- Qfo — Older alluvial-fan deposits (middle Pleistocene?)
- Qfo_1 — Older alluvial-fan deposits (middle Pleistocene?)
- Qfo_2 — Older alluvial-fan deposits (middle Pleistocene?)
- Qfo_3 — Older alluvial-fan deposits (middle Pleistocene?)
- Qfo_4 — Older alluvial-fan deposits (middle Pleistocene?)
- Qmls — Mega-landslide deposit (middle Pleistocene?)

FAULT BRECCIA

- QTbx — Fault breccia (Quaternary to Miocene?)

TERTIARY SEDIMENTARY ROCKS

- Ts — Tertiary sedimentary rocks, undivided (Pliocene to Miocene)

CENOZOIC AND CRETACEOUS IGNEOUS ROCKS

- Tb — Aphyric basaltic dikes (middle Miocene)
- Trcp — Coarsely porphyritic rhyolite [Jarbidge-type] (Miocene)
- Trfp — Finely porphyritic rhyolite [Jarbidge-type] (Miocene)
- Tmg — Biotite monzogranite orthogneiss (early Oligocene to middle Eocene)
- Tgd — Granodiorite (middle Eocene)
- Tgo — Granitic orthogneiss (middle Eocene)
- Tqd — Hornblende-biotite quartz dioritic orthogneiss (middle Eocene)
- TKlg — Leucogranite and leucogranitic orthogneiss (Oligocene to Cretaceous)

UNMETAMORPHOSED PALEOZOIC SEDIMENTARY ROCKS

- Pu — Sedimentary rocks, undivided (Permian)
- IPe — Ely Limestone (Pennsylvanian)
- Mdp — Diamond Peak Formation (Mississippian)

METAMORPHOSED PALEOZOIC AND NEOPROTEROZOIC SEDIMENTARY ROCKS

- Mc — Metapelite (Mississippian?)
- Msq — Schist and quartzite paragneiss (Mississippian?)
- Dg — Guilmette Formation (Devonian)
- DOd — Dolomite and marble (Devonian to Ordovician)
- Oe — Metamorphosed Eureka Quartzite (Ordovician)
- O€m — Impure calcite marble (Ordovician to Cambrian)
- O€mi — Intruded impure calcite marble (Ordovician to Cambrian)
- €Zpm — Metamorphosed Prospect Mountain Quartzite (Cambrian to Neoproterozoic) and McCoy Creek Group (Neoproterozoic)
- €Zpmi — Intruded metamorphosed Prospect Mountain Quartzite (Cambrian to Neoproterozoic) and McCoy Creek Group (Neoproterozoic)
- Zmu — Metamorphosed McCoy Creek Group, undivided (Neoproterozoic)
- Zmm — McCoy Creek Group marble (Neoproterozoic)

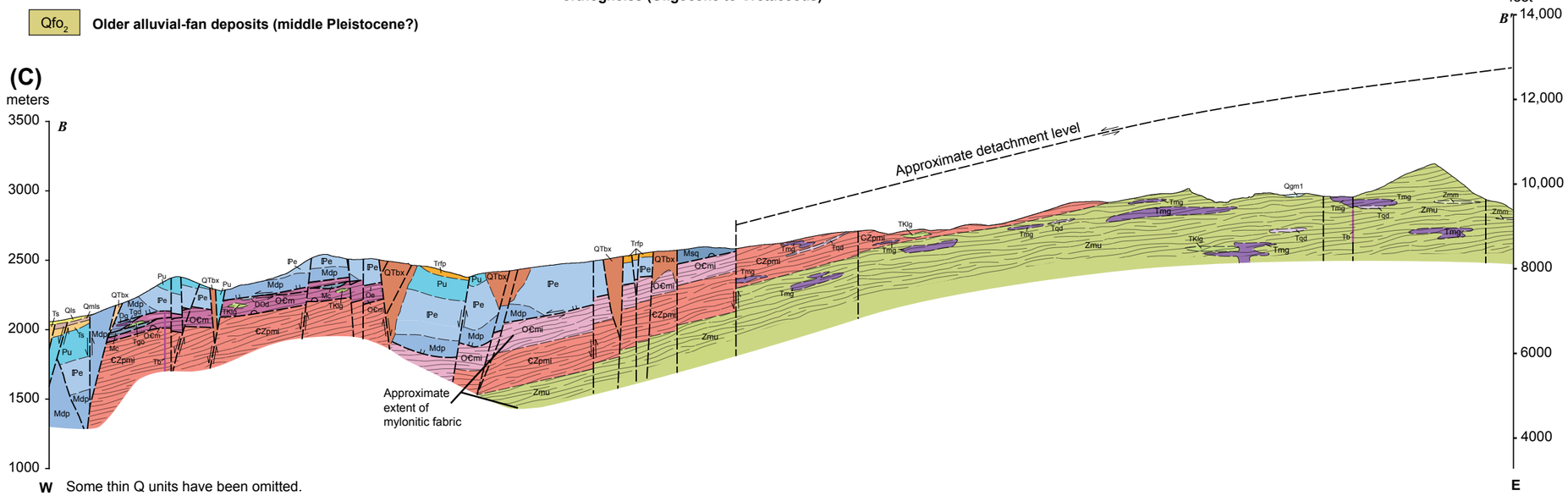

Figure 3 (*Continued*).

TABLE 1. SUMMARY OF TIMING CONSTRAINTS FOR BRITTLE VERSUS DUCTILE DEFORMATION IN THE EAST HUMBOLDT RANGE

	Data type	Age constraint	Description	Reference
Constraints on the timing of mylonitic shear zone activity	Deformed pluton	After ca. 29 Ma	Deformed Oligocene (ca. 31–29 Ma) monzogranite with similar fabrics and kinematics to all lower-plate mylonite rocks	Wright and Snoke (1993); Zuza et al. (2022a)
	Thermochronology	Before 25–22 Ma	Lower-plate muscovite and biotite $^{40}Ar/^{39}Ar$ dates and overlapping titanite, apatite, and zircon fission-track ages suggest that the shear zones cooled below ~300 °C by 22 Ma	Dallmeyer et al. (1986); Dokka et al. (1986); McGrew and Snee (1994); Gifford et al. (2008)
	Crosscutting dike	Before ca. 17 Ma	Undeformed subvertical basalt dike with chilled margins crosscuts shear zone	This study; Snoke (1980)
Constraints on the timing of brittle faulting	Detachment cuts dike	Possibly before and definitely after ca. 17 Ma	Detachment fault truncates basalt dike with chilled margins	This study; Snoke (1980)
	Brittle fractures intruded by basalt dikes	At ca. 17 Ma	Brittle subvertical fractures intruded by basalt dikes	This study
	Synkinematic basin	Initiated ca. 16 Ma and continued through late Miocene	Humboldt Formation is interbedded with ca. 15.3 Ma Jarbidge rhyolite, commonly exhibits growth strata, is often deformed by normal faults, and is associated with mid-Miocene extension across northeast Nevada	Satarugsa and Johnson (2000); Wallace et al. (2008); Colgan and Henry (2009); Colgan et al. (2010); Henry et al. (2011); Lund Snee et al. (2016); Camilleri et al., (2017); Zuza et al. (2021b)
	Low-temperature thermochronology	Initiated at ca. 17 Ma	Apatite fission-track and (U-Th)/He thermochronology from the southern Ruby Mountains records rapid cooling at ca. 17–15 Ma	Colgan et al. (2010)

Humboldt Formation (Sharp, 1939; Smith and Ketner, 1978) that spans ca. 16 Ma to 8 Ma (Wallace et al., 2008; Lund Snee et al., 2016; Camilleri et al., 2017; Zuza et al., 2021a). This diverse stratigraphy consists of sedimentary, volcaniclastic, and tuff deposits. Its deposition corresponds to the initiation of widespread Basin and Range extension in northeast Nevada, receiving sediments eroded from normal-fault–related uplifts (Colgan and Henry, 2009; Henry et al., 2011). The sequence is up to 5 km thick in Lamoille Valley with possible tilt-fanning observed in seismic data suggestive of synkinematic deposition (Satarugsa and Johnson, 2000; Colgan et al., 2010).

In the study area, these Humboldt Formation deposits contain the ca. 16–15 Ma Jarbidge-type rhyolite (Coats, 1987; Brueseke et al., 2014). These rhyolites are the southwesternmost known occurrences of Jarbidge-type rhyolites, which have distinctive phenocrysts and chemical characteristics (Coats, 1987; Brueseke et al., 2014). Jarbidge rhyolite is most extensive near Jarbidge, Nevada, near the Idaho border, where individual flows are more than 200 m thick, and cumulative sections are at least 480 m thick (Brueseke et al., 2014). These rhyolites are thought to have formed synchronously with the earliest phases of mid-Miocene Basin and Range extension (Colgan and Henry, 2009; Brueseke et al., 2014), which is consistent with their locations in the lower part of the synextensional Humboldt Formation.

The East Humboldt Range and Ruby Mountains are bounded by the Quaternary active, west-dipping Ruby Mountains fault zone on the western flank (Fig. 1) and the seemingly less recently active, east-dipping Ruby Valley fault zone on the eastern flank. The Ruby Mountains fault zone continues south along the western flank of the Ruby Mountains for >60 km (e.g., Colgan et al., 2010; Wesnousky and Willoughby, 2003). In the southern Ruby Mountains, high-angle faults associated with the Ruby Mountains fault zone are interpreted to cut the lower-angle Ruby Mountain–East Humboldt Range detachment fault (Colgan et al., 2010). Quaternary faults that bound the western East Humboldt Range similarly appear to cut any preexisting low-angle faults exposed at the surface (Zuza et al., 2022a). Therefore, the Quaternary history of high-angle faulting is not interpreted to be the modern expression of Miocene detachment faulting.

GEOLOGIC MAPPING IN THE EAST HUMBOLDT RANGE

New Geologic Mapping

New geologic mapping in the East Humboldt Range was conducted in 2019–2021 (Fig. 3). Herein, we focus on 1:24,000 scale geologic mapping of the Tent Mountain quadrangle (Zuza et al., 2021a) with a particular emphasis on the southern half, which exposes the upper plate of the detachment fault. This region was mapped earlier by Snoke (1980) and as part of an M.S. thesis by Hurlow (1987). Our final georeferenced 7.5′ quadrangle geologic map is available at https://pubs.nbmg.unr.edu/Geol-Tent-Mountain-quad-p/of2021-03.htm.

Geologic Units

Lower-plate bedrock units are summarized in Figure 4 and in Zuza et al. (2021a, 2022a). These consist of metamorphosed and mylonitized Proterozoic–Paleozoic sedimentary rocks. Voluminous Cretaceous–Cenozoic igneous rocks intrude

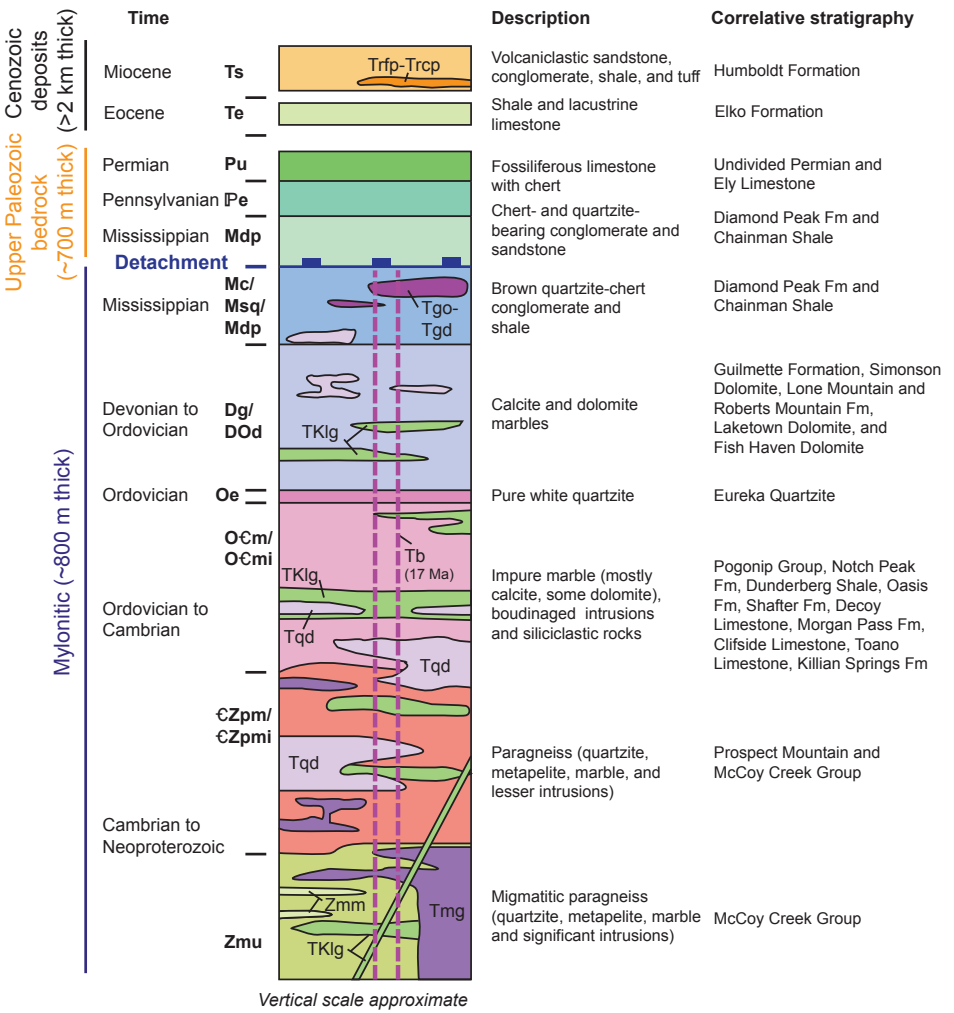

Figure 4. Interpretive stratigraphic column of the study area, displaying crosscutting relationships of igneous intrusions, main rock types, and correlations with regional Neoproterozoic–Paleozoic stratigraphy, modified from Zuza et al. (2022a). Fm—Formation.

the paragneiss bedrock, often comprising more than two thirds of the bedrock by volume. Map units are assigned and named based on the host-rock protolith, following the approach used in the Ruby Mountains–East Humboldt Range since Howard (1966, 1971).

The oldest and structurally deepest rocks are the Neoproterozoic McCoy Creek Group (Zmu) quartzite, schist, and marbles and Neoproterozoic–Paleozoic Prospect Mountain Quartzite (€Zpm). Discontinuous meter-scale lenses of marble (Zmm) were observed within Zmu. Above €Zpm, there are Cambrian–Ordovician impure marbles (O€m and O€mi) that contain diverse calcite and dolomite marbles, calc-silicate, and pelitic layers with variable deformation and boudinage of intruded igneous rocks. Above O€m, but commonly observed tectonically interwoven within the marbles, there is the Ordovician Eureka Quartzite (Oe). Above the Eureka Quartzite, there are marbles and dolomite of the mixed Devonian–Ordovician marble and dolomite unit (DOd). Distinctive white-blue color-banded, finely laminated, and graphite-bearing marbles were mapped as the Devonian Guilmette Formation (Dg) (e.g., Snoke, 1980).

In the undeformed regional stratigraphy, there is a thick package of Mississippian shale and conglomerate above the Devonian Guilmette Formation. In the study area, these rocks are exposed in two varieties: One is strongly lineated and fine grained (Mc and Msq units), and the other is generally undeformed conglomerate of the Mississippian Diamond Peak Formation (Mdp). The dark-brown fine-grained Msq unit was particularly enigmatic, but detrital zircon analyses suggested that the unit is correlative to other Mississippian strata (Zuza et al., 2022a). Mc and Msq are strongly recrystallized, but they broadly correlate with the Chainman Shale and the Diamond Peak Formation. In several outcrops, elongate ~1–4-cm-long blue-white ellipses are interpreted to represent flattened and stretched conglomerate clasts (Figs. 5A and 5B; Hurlow, 1987). The undeformed Diamond Peak Formation represents the structurally lowest part of the upper-plate stratigraphy, which is separated from the mylonitic lower plate by a detachment fault. The unit resembles other Mississippian Diamond Peak Formation rocks in northeast Nevada, with reddish brown chert-pebble conglomerate with well-rounded clasts up to ~10 cm diameter (mostly <6 cm; Fig. 5C). Clasts are composed of colored chert or quartzite.

Above the Mississippian Diamond Peak Formation in the upper plate, there are Pennsylvanian Ely Formation (IP) and undifferentiated Permian strata (Pu). The Ely Formation consists of massive to medium-bedded gray limestone with darker chert layers and bioclastic limestone with brachiopod fauna, crinoid columnals, and other fossil fragments. The undifferentiated Permian rock is

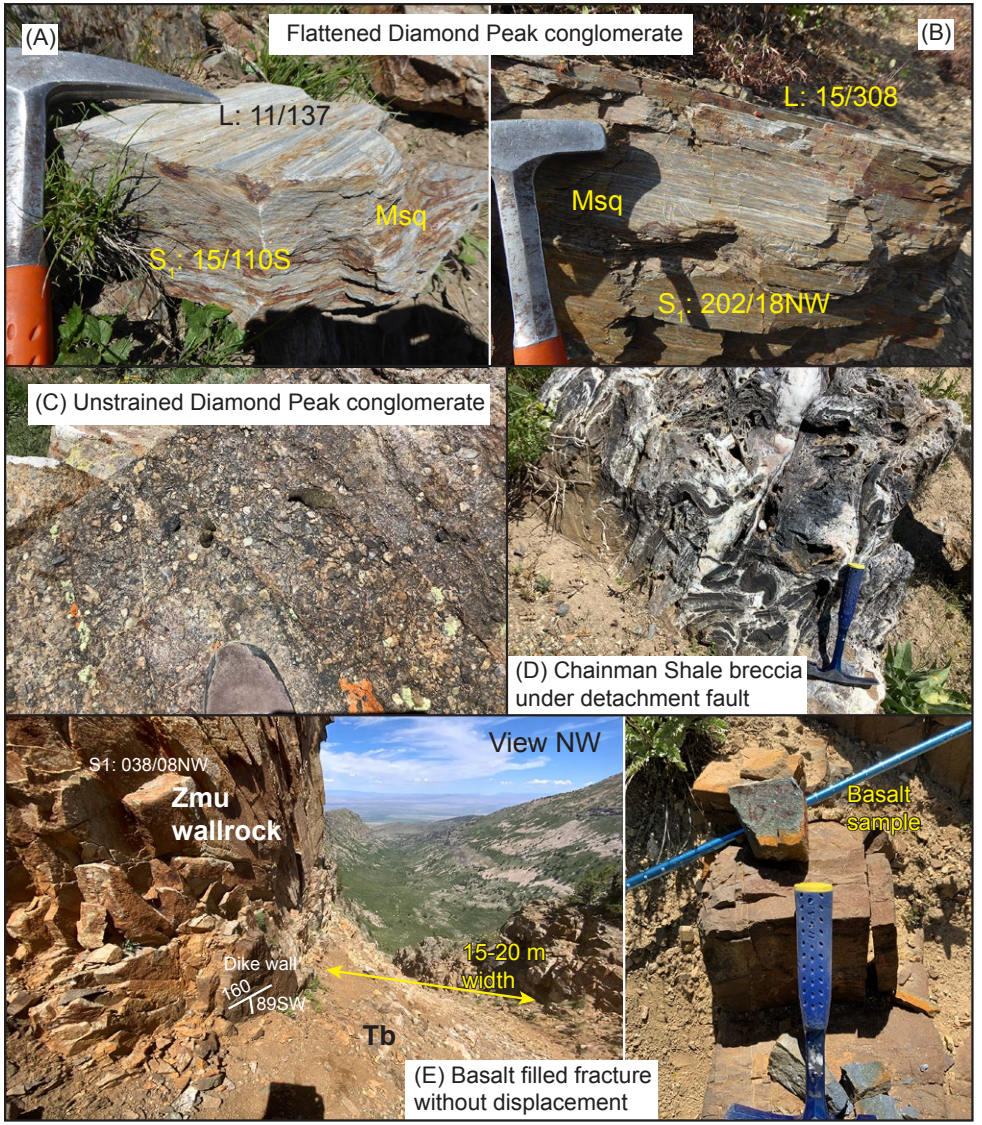

Figure 5. Field photographs, with locations provided in Figure 3A. (A–B) Flattened and stretched Mississippian Diamond Peak conglomerate. Different-colored lenses are probably different chert and quartzite pebbles. (C) Undeformed, but silicified, Diamond Peak conglomerate from upper-plate rocks. (D) Outcrop of brecciated Chainman Shale in the Ruby Mountains–East Humboldt Range detachment fault. Note white quartz veining. (E) Undeformed basalt dike filling into large NW-striking fracture. Msq—Mississippian schist-quartzite unit; Tb—Tertiary basalt dike; Zmu—Neoproterozoic McCoy Creek Group, undifferentiated.

limestone, cherty limestone, sandstone, and limestone conglomerate. Snoke (1980) and Zuza et al. (2021a) presented fossil age constraints to differentiate these units and confirm their ages.

The voluminous igneous rocks in the study area provide important constraints on the timing of Ruby Mountains–East Humboldt Range metamorphic core complex development. Here, we introduce them from oldest to youngest using age constraints from this study and other sources (e.g., Wright and Snoke, 1993; Zuza et al., 2022a). These include a Cretaceous–Tertiary leucogranite (TKlg), Eocene quartz diorite (Tqd), Eocene granodiorite (Tgd), Eocene granitic orthogneiss (Tgo), Oligocene monzogranite (Tmg), Miocene basalt (Tb), and Miocene rhyolite (Trfp and Trcp). TKlg forms discontinuous meter- to submeter-scale concordant sheets, pods, or lenses of leucogranite throughout the lower-plate rocks in the metamorphic core complex. Most zircon ages from TKlg span ca. 85–80 Ma (McGrew et al., 2000; Hallett and Spear, 2015), but observations of similar-looking leucogranite intermingled with, or directly crosscutting, the Eocene quartz diorite and Oligocene monzogranite intrusions require that the TKlg age range extends to as young as Oligocene (Zuza et al., 2022a). Eocene–Oligocene monazite ages from the East Humboldt Range are interpreted to reflect retrograde metamorphism due to magmatism and partial melting (Hallett and Spear, 2015), which supports a complex Cretaceous–Cenozoic melt history.

The quartz diorite has been previously described by McGrew (2018) and Zuza et al. (2022a). It is weakly to strongly foliated and lineated, and it has a porphyritic texture with 1–2 mm plagioclase and lesser hornblende, biotite, and quartz. U-Pb zircon ages span ca. 40–38 Ma (Zuza et al., 2022a). The Tertiary granodiorite (Tgd) and granitic orthogneiss (Tgo) units were not previously well described in the literature, and their zircon ages are reported in this study. Tgd is undeformed equigranular granodiorite with no evidence for crystal-plastic deformation. The unit is fractured, brecciated, and chlorite-altered, probably due to the nearby, structurally higher, detachment fault. Tgd is similar to the granodiorite of the Eocene (ca. 36 Ma) Harrison Pass pluton (Barnes et al., 2001) to the south in the Ruby Mountains.

The granitic orthogneiss (Tgo) is moderately foliated, usually weakly lineated, coarse- to medium-grained monzogranitic orthogneiss composed of plagioclase, K-feldspar, quartz, biotite, and muscovite, with relatively unique plagioclase augen. This rock is commonly chlorite-altered, and exposures generally have a green hue. This unit is very localized, with most exposures in the southwest corner of the geologic map (Fig. 3) and in the Gordon Creek quadrangle to the southeast, where it was mapped as the biotite granodiorite-monzogranite orthogneiss of Horse Creek by Sicard and Snoke (2020).

Basalt dikes (Tb) are gray-black undeformed, nonfoliated, microcrystalline tholeiitic basalt to basaltic andesite. Most exposures strike north-northwest, are ≤1 m wide, and discordantly crosscut adjacent units, including mylonitic foliations. Local chilled margins are observed. Ages span ca. 17–15 Ma based on $^{40}Ar/^{39}Ar$ dating in the map area and in Angel Lake to the northeast (Zuza et al., 2021b; Dee et al., 2015).

Rhyolite lavas are divided into finely (Trfp) and coarsely (Trcp) porphyritic phases that are orange- to pinkish-gray. Both units contain 25%–30% phenocrysts of distinctive smoky quartz, sanidine, plagioclase, and clinopyroxene. Phenocrysts are <2 mm in diameter in finely porphyritic rhyolite and commonly 6 mm and up to 12 mm in diameter in the coarsely porphyritic rhyolite. The rhyolite is interbedded with the Miocene Humboldt Formation. Trcp defines 30–50 m cliff bands (Zuza et al., 2021a), whereas Trfp is more discontinuously exposed as thin deposits. Similar Jarbidge-type rhyolites are present along the east side of the East Humboldt Range in the Welcome and Humboldt Peak quadrangles (McGrew and Snoke, 2015; McGrew, 2018). The $^{40}Ar/^{39}Ar$ anorthoclase ages are 15.33 ± 0.01 Ma and 15.37 ± 0.04 Ma for Trcp and Trfp, respectively (Zuza et al., 2021a; Snoke et al., 2021), which overlap other $^{40}Ar/^{39}Ar$ ages from Jarbidge-type rhyolites documented by Coats (1987) and Brueseke et al. (2014).

Field Relationships

The overall structural framework of the study area (Fig. 3) is gently west dipping, so that the eastern part of the map area exposes structurally deeper mylonitic and migmatitic rocks, including Neoproterozoic–Paleozoic paragneiss and voluminous deformed intrusions (e.g., McGrew et al., 2000; McGrew, 2018). The lower-plate paragneiss and intrusions are severely attenuated into an ~1-km-thick mylonitic shear zone. Lineations trend WNW (~285°–290°), with most foliations being subhorizontal to gently west dipping (Fig. 3). In the study area, all rocks show top-to-the-WNW shear kinematics (e.g., Hurlow et al., 1991; Zuza et al., 2022a). The structurally highest parts of the mylonitic shear zone, developed in Neoproterozoic–Paleozoic paragneiss, are generally located to the west, where the primary detachment fault separates unmetamorphosed Mississippian through Permian upper-plate rocks from the mylonite zone. Miocene-to-present west-dipping normal faults drop Miocene basin sediments against this metamorphic core complex.

Across the map area, there is a network of parallel NNW–striking subvertical fractures or faults that cut across the valleys and ranges. In detail, those in the east have a northwest strike, and those in the west strike north. We believe this distinction is significant because those in the east (1) have very minor to negligible offset <1 m and (2) are intruded by undated, but probably middle Miocene, basalt dikes (between Second and Third Boulder Creeks in Fig. 3; see also Fig. 5E). Conversely, the steep faults in the west have variable displacement, ranging from ~1 m to tens of meters, and they parallel the Quaternary range-front normal-fault system.

The eastern northwest-striking fractures that are variably intruded by basalt dikes probably formed ca. 17–15 Ma because all dated basalt dikes in the area are this age. These fractures have negligible observed displacement across them, and therefore we interpret these structures as mode-1 opening fractures, with possible minor shear displacement. These tensile fractures may have developed in an early phase of brittle extension, coeval with the intrusion of 17–15 Ma basalt dikes. The rare basalt dikes in the western map area strike northwest, oblique to the prominent north strike of brittle normal faults, thus implying that this northwest-striking generation of faults and diking may be related.

The north-striking faults in the western map area have mapped normal-sense displacements, but they do not have age constraints. They parallel the range front, and in a few locations, the projection of concealed faults suggests they should postdate the eastern northwest-striking fracture network. Therefore, we interpret the north-striking fault generation to postdate the ca. 17–15 Ma northwest-striking fracture generation. The north-striking, subvertical-to-west-dipping fault network that parallels the western range front was probably generated during more recent late Miocene to present normal faulting. Some of these faults involve silicified breccia, and these silicified deposits are observed parallel and close to the range front, as observed just south of Reed Creek in Figure 3. The range-front west-dipping normal faults have progressively stepped westward. Miocene sediments are faulted against the higher-relief bedrock of the East Humboldt Range, and to the west of this fault, there is another normal fault that bounds the western extent of uplift of Miocene sedimentary rocks (Figs. 1 and 3). Together, these two normal faults have bounded a broadly folded Miocene section, although poor exposure limits our ability to resolve map-scale structures or folds in this section.

Some of the most important, yet ambiguous field relationships are observed in the Dorsey Creek drainage, and therefore we focus herein on observations from this drainage. An enlarged geologic map of Dorsey Creek is presented in Figure 6. At the drainage scale, the structurally deepest rocks consist of heavily intruded, mylonitic €Zpmi that is rich in pelitic material and thus may represent Neoproterozoic McCoy Creek Group rocks. These rocks are overlain by deformed O€m marbles potentially across a low-angle ductile fault, as interpreted by Snoke (1980) on the basis of O€m marbles placed atop possible McCoy Creek Group rocks, thus omitting the Neoproterozoic–Cambrian Prospect Mountain Quartzite. Slices of Eureka Quartzite and Mississippian Chainman Shale are tectonically interwoven with the deformed marbles. Structurally higher, there are blue-white banded marbles interpreted as Devonian Guilmette Formation. Upper-plate Mississippian Diamond Peak through undifferentiated Permian strata are juxtaposed against these

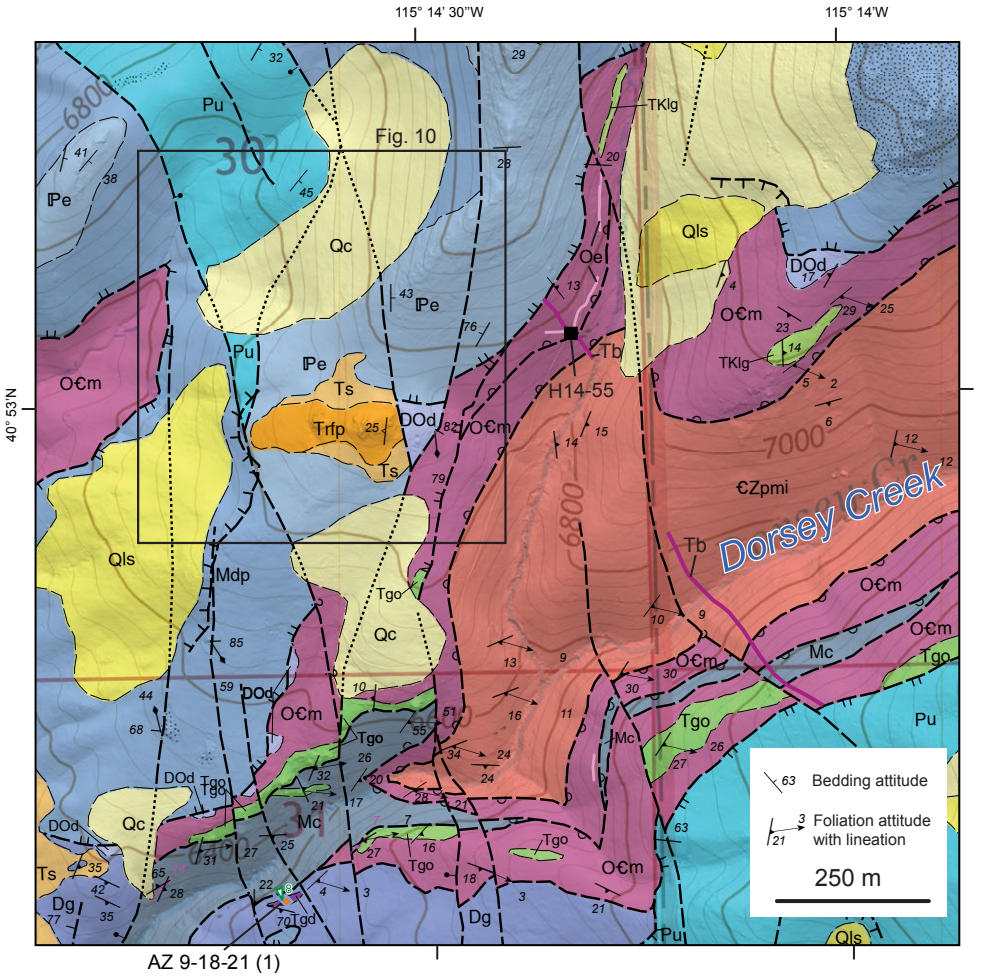

Figure 6. Enlarged part of the geologic map around Dorsey Creek. Location and map symbols are shown in Figure 3.

mylonitic units across the main Ruby Mountain–East Humboldt Range detachment fault. Discontinuous exposures of white dolomite (DOd) are found scattered along the detachment fault (Fig. 6).

Throughout the drainage, deformed marbles, which are probably Devonian to Cambrian in age, are located structurally above Mississippian Chainman Shale (Mc), which is an older-over-younger thrust-like relationship (Figs. 7A and 7B). However, asymmetric fabrics throughout this drainage suggest a most-recent phase of top-to-the-W shear that was parallel to the inferred mylonite and detachment kinematics throughout the East Humboldt Range. This includes 5-m-scale top-to-the-W asymmetric folds in the Chainman Shale (Fig. 7G) and top-to-the-W mica fish viewed in photomicrograph (Fig. 7H).

The deformed marbles in Dorsey Creek are intruded by the slightly foliated, cliff-forming orthogneiss (Tgo). At one location, a ramp-flat relationship is clearly visible with truncated Tgo bodies (Figs. 7A and 7B). The ramp-flat relationship is consistent with either top-to-the-W normal faulting or top-to-the-E thrusting. However, as stated above, meso- and microscale finite strain observations support top-to-the-W shear during the normal-sense phase of deformation.

A particularly important outcrop is on the southern flank of Dorsey Creek (Figs. 8 and 9), where the Devonian Guilmette Formation and O€m marbles are atop Mississippian Chainman Shale. Specifically, the Devonian Guilmette Formation is intruded by undeformed granodiorite, Tgd, with undulous, intrusive contacts (Figs. 9A–9C). The structural relationships imply an older-on-younger thrust fault with the Dg-O€m over Mc. The mylonitic Dg is intruded by undeformed granodiorite, thus requiring shearing of the Dg prior to the intrusion of Tgd. Alternatively, these relationships could be interpreted to reflect rheologic contrasts between the weaker shale/marble rocks versus the granodiorite, such that the weaker phases absorbed all of the deformation. However, based on our mapping in and observations across the East Humboldt Range, we do not favor this scenario because almost all other igneous rocks, including diorites and granites, show significant deformation, even when surrounded by rheologically weaker shale and limestone marble units (e.g., Hurlow, 1987; Zuza et al., 2022a). The outcrop in Dorsey Creek appears to uniquely show the postkinematic intrusion of the Tgd unit. Local contact metamorphism of the Dg unit also indicates postkinematic intrusion of Tgd.

An ~1-m-wide, NW-striking undeformed basalt dike intruded the mylonitic rocks in Dorsey Creek (Figs. 3 and 6). The trace of this dike disappears moving across the main detachment fault into the upper-plate Paleozoic rocks. This relationship demonstrates that the detachment fault cuts the basalt dike, and, to our knowledge, basalt dikes are not observed in the upper-plate Paleozoic units in the range (e.g., Snoke, 1980; McGrew and Snoke, 2015; McGrew, 2018; this study).

The middle Miocene rhyolite flows were observed covering the mylonitic lower plate and possibly the detachment fault, which is important for

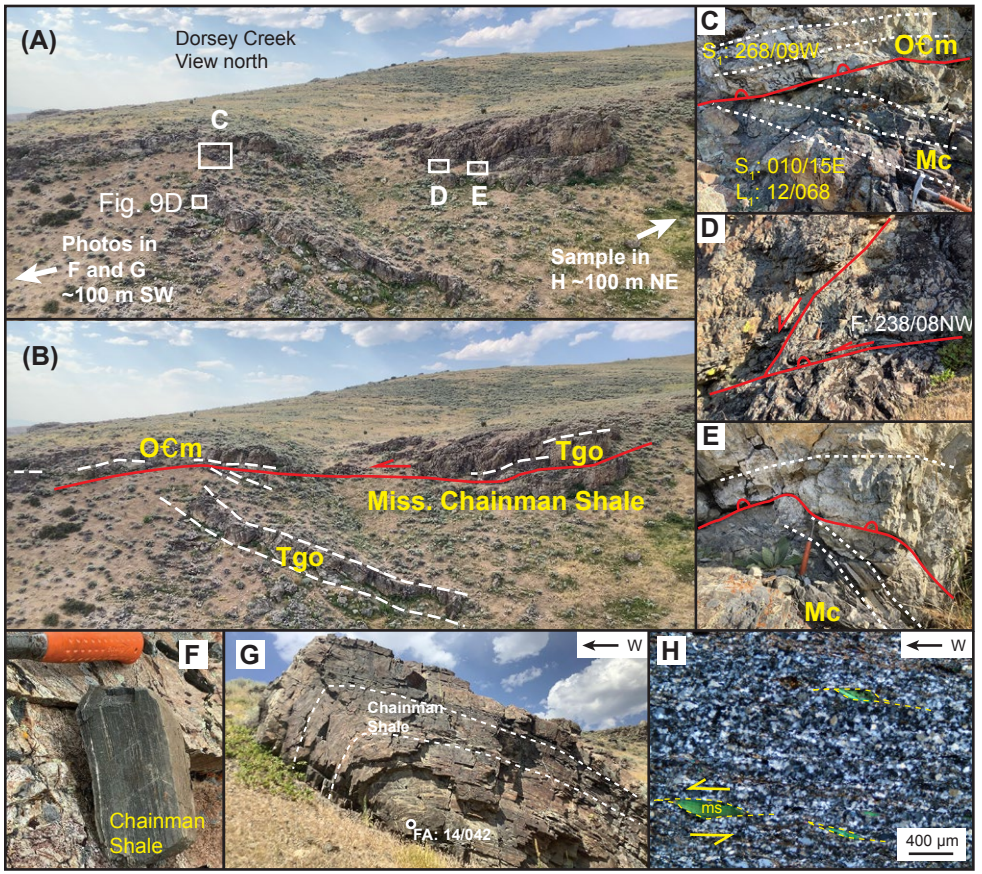

Figure 7. Field photographs, with locations provided in Figure 3A. (A) Uninterpreted and (B) interpreted photograph looking north across Dorsey Creek, showing hanging-wall flat and footwall ramp cutoff relationships. Hanging wall consists of deformed marbles and Tertiary granitic orthogneiss (Tgo) intrusions, whereas the footwall is mostly composed of Chainman Shale and Tgo intrusions. (C–E) Various fault relationships observed in the field along this detachment fault sliver suggesting top-to-the-W normal-sense displacement, as evidenced by hanging-wall flat and footwall ramp geometries (C, E) and synthetic west-directed subsidiary faults (D). (F) Chainman Shale in Dorsey Creek, which is (G) folded in an asymmetric west-vergent fold (FA—fold axis). (H) Photomicrographs show top-to-the-W muscovite (ms) mica fish in the Chainman Shale. O€m—Ordovician-Cambrian marble, Mc—Mississippian Chainman Shale.

interpreting the relative timing of detachment-fault activity. Specifically, poorly exposed rhyolite flows were originally mapped as hanging-wall rocks of the detachment (Fig. 3; Snoke, 1980; Hurlow, 1987). However, in our new geologic mapping, we mapped the rhyolite (Tr) and underlying Humboldt Formation (Ts) in depositional contact over the Paleozoic strata just west of Dorsey Creek (Fig. 6) and in depositional contact over lower-plate mylonitic marbles (O€mi and Dg) around Reed Creek (Fig. 3). This relationship is somewhat ambiguous in the field, but the best exposures are near Dorsey Creek (Figs. 6 and 10). Here, one can interpret this contact as either a depositional contact or detachment-fault contact (Fig. 10). Specifically, the rhyolite exposures are brecciated and altered (Figs. 10C and 10D), which could have resulted from adjacent high-angle faulting, inferred detachment faulting, or a combination of processes. Specifically, we note that the rhyolite exposure is bounded by high-angle normal faults that are associated with brecciation and silicification of the Upper Paleozoic rocks ~1 km north of the rhyolite exposure (Fig. 6). We did not observe compelling evidence for a detachment fault beneath the rhyolite exposures, and therefore we prefer a conservative interpretation where the rhyolite lavas and Miocene sediments were deposited over the exposed Paleozoic bedrock (Fig. 10A). The rhyolite was subsequently brecciated during late-stage high-angle normal faulting. Exposures of Miocene rhyolite mapped in the adjacent Secret Valley quadrangle (Snoke et al., 2022) with similarly ambiguous field relationships were interpreted as depositional on underlying lower-plate early Paleozoic marbles in part due to a discontinuous vitrophyre preserved at the base of the rhyolite outcrop. This mapping in Secret Valley therefore supports our interpretations of a depositional relationship between rhyolite and the older bedrock units.

The map exposures of rhyolite cover both lower-plate Paleozoic marbles (O€m/O€mi) and upper-plate Pennsylvanian Ely Limestone (ℙ) (Fig. 3). The depositional interpretation (Fig. 10A) suggests that detachment faulting brought Pennsylvanian Ely Limestone against deformed Paleozoic marbles, all of which were subsequently covered by Jarbidge-type rhyolite lavas. This depositional interpretation suggests that detachment faulting had initiated and slipped significantly by the time the rhyolite lavas were erupted (ca. 15.3 Ma), such that the upper and lower plates were against each other and exposed at the surface by ca. 15.3 Ma. Tertiary sediments and rhyolite onlapped these exposed lower-plate rocks. Detachment slip must have continued on another fault splay to rotate the Miocene rhyolite and Humboldt Formation, as observed in the Clover Creek area (Fig. 2; McGrew and Snoke, 2015). Conversely, the detachment-fault interpretation (Fig. 10B) requires that an initial phase of detachment faulting brought ℙ against O€mi, and a later phase of detachment faulting cut the earlier phase,

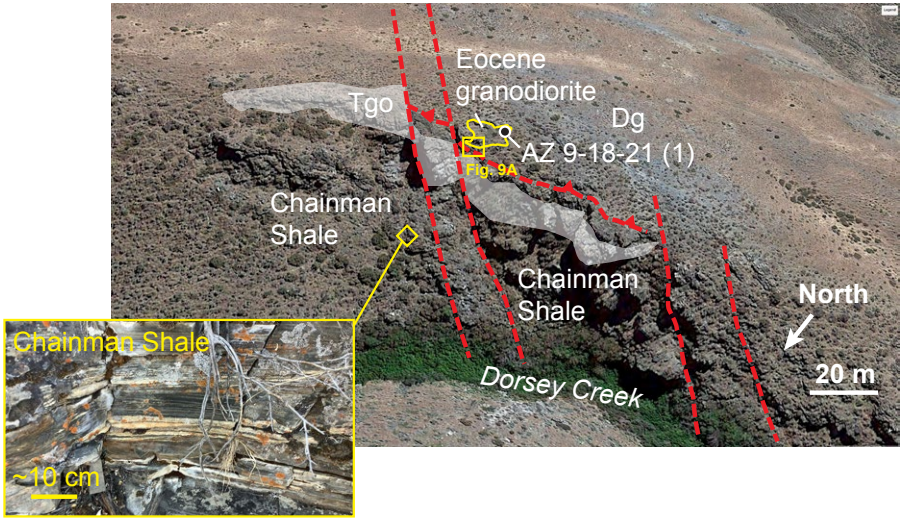

Figure 8. Google Earth image looking at the southern flank of Dorsey Creek, where the Devonian Guilmette Formation (Dg) is thrust over Mississippian Chainman Shale (Mc). This thrust is intruded by undeformed Eocene granodiorite (Tgd). Note: Several high-angle faults (red dashed lines) cut these outcrops. Tgo—Tertiary granitic orthogneiss.

to bring a hanging wall of rhyolite lavas against O€mi-ℙP. This model requires that significant faulting occurred after ca. 15.3 Ma. Both models have their own shortcomings: The depositional contact model suggests that most of the bedrock was exhumed over a very short time scale (17–15.3 Ma), which may be too rapid, whereas the detachment-fault model implies that most of the detachment slip occurred after 15.3 Ma, which is inconsistent with significant sedimentation and rapid cooling initiating at ca. 17–16 Ma (Table 1; Colgan et al., 2010). The relationships between the Tertiary rhyolite and the underlying lower-plate rocks are very important to understand for relative timing constraints on detachment faulting, and therefore we emphasize that these relationships are ambiguous (Fig. 10), and interpretations remain speculative.

U-Pb GEOCHRONOLOGY

We conducted U-Pb zircon dating on four igneous samples to constrain the age of deformed and undeformed intrusions (Table 2). We specifically focused on intrusions from structurally high levels of the lower plate to improve our relative timing constraints. Complete separation and analytical details are given in the Supplemental Materials.[1] Analyses were completed at the University of Nevada, Reno. Complete data tables and concordia plots for zircon analyses are available in the Supplemental Material, including Table S1 (see footnote 1).

In Dorsey Creek, in the southern part of the Tent Mountain quadrangle, rather unique intrusions were observed within slices of Paleozoic marbles. Sample AZ 6–8–21 (1) was collected from a small medium-grained equigranular leucogranite body mapped as TKlg that intruded O€m marbles (Fig. 3). The sample yielded relatively few zircon grains. Seven concordant analyses yielded a weighted mean age of ca. 37 Ma. No other Eocene dates have been reported from leucogranite bodies in the study area.

Just west of the previous sample, an undeformed granodiorite body (Tgd) intrudes mylonitic Devonian Guilmette Formation (Dg) marbles that were thrust over Mississippian Chainman Shale (Mc) (Figs. 6 and 8). Therefore, the age of the Tgd unit constrains a phase of shearing in the Dg. However, the undeformed Tgd does not directly crosscut the thrust fault relationship, and therefore there is no direct constraint on the age of thrusting. Sample AZ 9–18–21 (1) was collected from an ~10 m exposure of the Tgd body (Fig. 8). Twenty-two analyses yielded concordant ages clustered at ca. 39 Ma. This sample yielded a weighted mean age of 39.1 ± 1.2 Ma (mean square of weighted deviates [MSWD]: 0.61), which implies that some phase shearing occurred during or prior to the Eocene.

To the north of Reed Creek, the moderately foliated coarse granite, mapped as Tgo, intrudes the schist and quartzite Msq unit. Sample AZ 6–6–21 (1) was collected from the Tgo unit. Twenty concordant analyses clustered near ca. 39 Ma, yielding a weighted mean age of 38.9 ± 1.2 Ma (MSWD: 0.61).

In the Soldier Peak quadrangle just south of our study area, Snoke et al. (2022) mapped a unit referred to as the granitic orthogneiss of Secret Peak (their unit Tgs). A sample from this unit, AZ 7–15–21 (3), yielded 20 concordant U-Pb analyses, with a weighted mean age of 30.9 ± 0.9 Ma (MSWD: 0.93). This age is consistent with isotope dilution–thermal ionization mass spectrometry (ID-TIMS) ages from two zircon fractions by Wright and Snoke (1993) that yielded nearly concordant ages of ca. 32 Ma without stated uncertainty. This age suggests a genetic association with the widespread Oligocene monzogranite (Tmg) unit.

DISCUSSION

Structural Geometries and Restoration of the Detachment-Fault System

An east-west–oriented cross section across the southern East Humboldt Range (Fig. 3B) conveys the relationships between the mylonitic lower plate

[1]Supplemental Material. Details of U-Pb zircon dating, complete datatables of U-Pb zircon dating, and a compilation of muscovite and biotite Argon dates. Please visit https://doi.org/10.1130/GEOS.S.23290280 to access the supplemental material, and contact editing@geosociety.org with any questions.

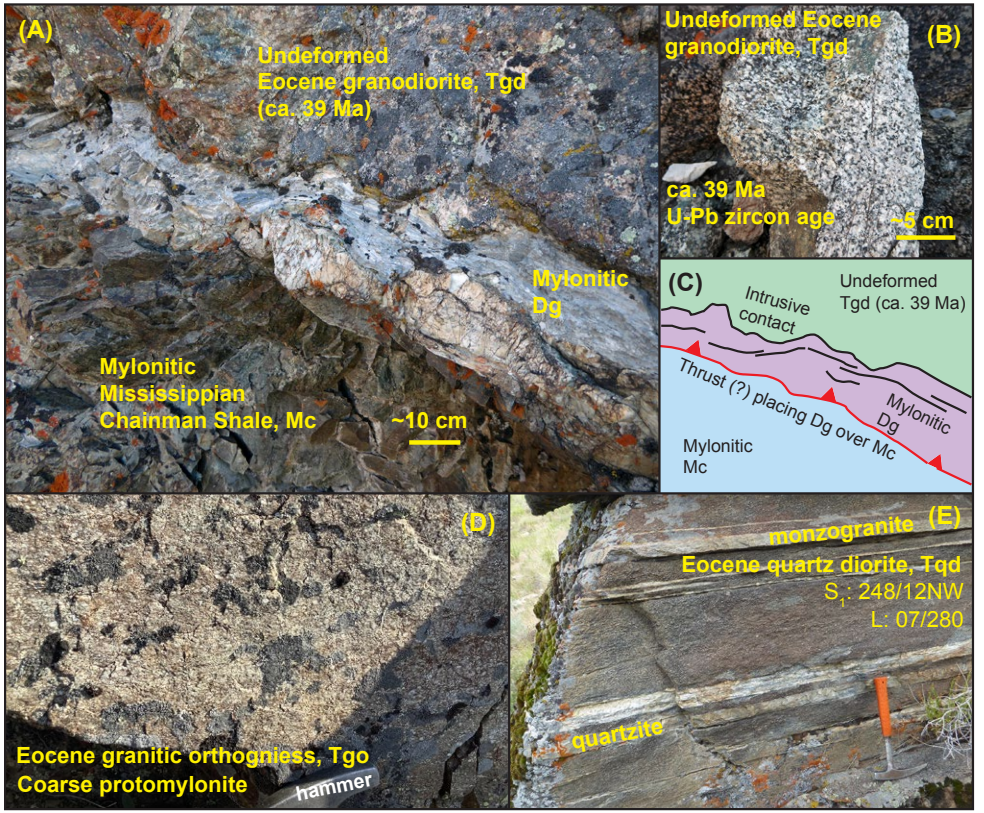

Figure 9. Field photographs of diverse Eocene igneous rocks in the study area. (A) Eocene granodiorite intrusion (Tgd) intruding mylonitic and deformed Guilmette Formation (Dg) and Mississippian Chainman Shale (Mc). Location is shown in Figure 7. (B) Fresh surface of Tgd showing its undeformed character. (C) Interpretative sketch of A. This thrust fault may have been reactivated and deformed by Cenozoic normal-sense shearing. (D) Moderately deformed and weakly lineated Eocene granitic orthogneiss (Tgo), which differs from strongly mylonitized igneous rocks and paragneiss exposed across much of the East Humboldt Range. (E) Foliated Eocene quartz diorite (Tqd) showing white feldspar phenocrysts with bands of monzogranite and quartzite that were sheared together (photo location: 40°57′7.45″N, 115°13′15.03″W).

and brittlely deformed upper plate. In the east, the Neoproterozoic through Ordovician paragneiss sequence is deformed in an ~1-km-thick mylonitic shear zone that is heavily intruded by concordant, foliation-parallel sills of Cretaceous–Cenozoic leucogranite (TKlg), Eocene quartz diorite (Tqd), and Oligocene monzogranite (Tmg). The host-rock paragneiss and the intrusions are deformed similarly, as evidenced by parallel foliations, lineations, and observed top-to-the-W shear kinematics. The western part of the study area exposes the brittle detachment fault as it intersects topography. The detachment generally truncates O€mi and does not obviously cut up or down the footwall section within the map area (Fig. 3B). The hanging wall consists of Mississippian Diamond Peak Formation, Pennsylvanian Ely Limestone, and undifferentiated Permian strata. The detachment fault is mostly parallel to the stratigraphically oldest Mississippian Diamond Peak Formation, but it cuts up section in the hanging wall through the Pennsylvanian Ely Limestone in several locations (Fig. 3).

In the western part of the cross section, there are complex detachment-fault slivers of mapped Mississippian Chainman Shale, Ordovician Eureka Quartzite, and early Paleozoic marbles (O€m) with lesser strained Tertiary granodiorite and granitic orthogneiss (Tgd and Tgo) between the upper and lower plates. These rocks are best exposed in Dorsey Creek, and their relationships are enigmatic. As discussed above, because of complex older-over-younger and younger-over-older field relationships, we interpret that this fault-bounded package of rocks represents an earlier thrust system that was later deformed via normal-sense Oligocene shearing and middle Miocene detachment faulting. The unit juxtaposition is broadly reflective of normal-fault relationships, with the least-deformed rocks (i.e., undifferentiated Permian to Mississippian Diamond Peak) faulted against the moderately deformed sliver (i.e., Chainman Shale, Eureka Quartzite, Paleozoic marbles, and Eocene granodiorite/orthogneiss), which overlies the Cambrian–Neoproterozoic paragneiss (€Zpmi-Zmu) mylonites. The Mc-O€m sliver was juxtaposed against the €Zpmi-Zmu mylonites prior to the intrusion of a middle Miocene basalt dike because the basalt dike intrudes the fault contact of these units in Dorsey Creek (Fig. 6).

Although the Chainman Shale is limited in the map area, it was commonly observed as thin exposures, lag, or rare outcrops near the detachment fault. For example, there is a Chainman Shale breccia exposure in Figure 5D or a small window of Chainman Shale mapped beneath the detachment just southeast of Dorsey Creek (Fig. 3A). Therefore, we interpret that the shale served as an important guide to focus detachment faulting, which explains why the stratigraphically lowest, upper-plate unit observed was the Mississippian Diamond Peak Formation, which stratigraphically overlies the Mississippian Chainman Shale. These observations also demonstrate that the detachment fault did not significantly omit stratigraphic section, similar to the northern Snake Range to the south (Miller et al., 1983).

In Figure 11, we provide a simple reconstruction of the main cross section. Although the upper-plate

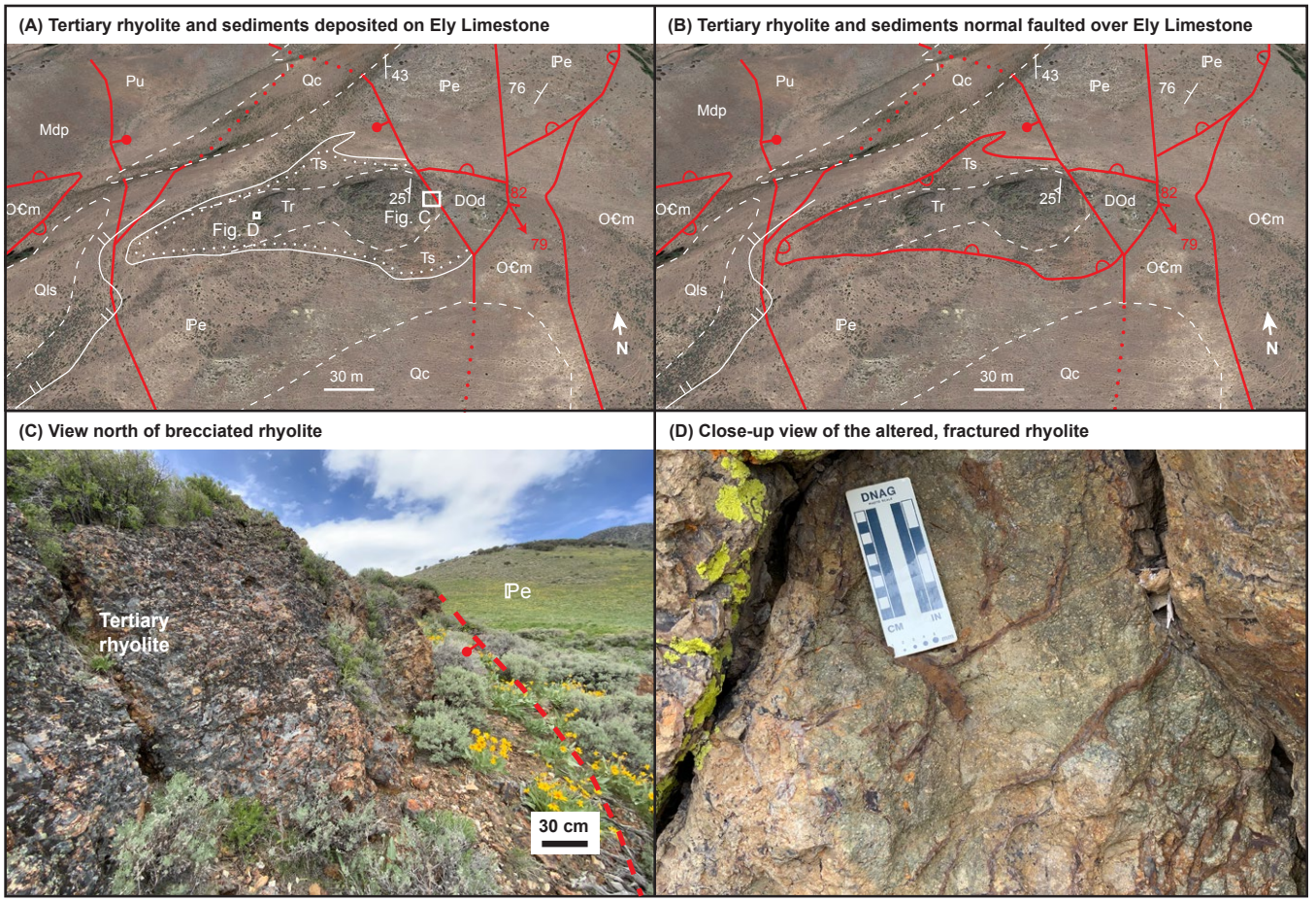

Figure 10. Exposures of Tertiary rhyolite in the western part of the study area just north of Dorsey Creek (location in Fig. 6). (A) Sketch geologic map over an oblique Google Earth image showing our interpreted map relationships with a depositional contact between the Tertiary rhyolite (Tr) and sediments (Ts) overlying Ely Limestone (IPe) and (B) an alternative interpretation where the rhyolite and sediments are in detachment fault contact with the limestone. Symbology is the same as in Figures 3 and 6, except the dot-adorned contact that symbolizes an unconformity. (C–D) Field photographs showing a view of the brecciated rhyolite adjacent to a down-to-the-W normal fault (C) and the altered, green-hued fractured rhyolite (D). IPe—Ely Limestone.

TABLE 2. NEW U-Pb ZIRCON GEOCHRONOLOGY RESULTS FROM THE RUBY MOUNTAINS–EAST HUMBOLDT RANGE METAMORPHIC CORE COMPLEX

Sample	Unit	Latitude (°N)	Longitude (°W)	Weighted mean age	*n*
AZ 6-8-21 (1)	Leucogranite (TKlg)	40.88060	115.22516	36.8 ± 1.0 Ma (MSWD: 0.30)	7
AZ 9-18-21 (1)	Granodiorite (Tgd)	40.87587	115.24463	39.1 ± 1.2 Ma (MSWD: 0.61)	22
AZ 6-6-21 (1)	Granitic orthogneiss (Tgo)	40.91322	115.22119	38.9 ± 1.2 Ma (MSWD: 0.87)	20
AZ 7-15-21 (3)	Granitic orthogneiss of Secret Peak (Tgs in Snoke et al., 2022)	40.82692	115.25543	30.9 ± 0.9 Ma (MSWD: 0.93)	20

Notes: MSWD—mean square of weighted deviates.

rocks are heavily faulted, the mapped structural thickness of Mississippian Diamond Peak through undifferentiated Permian strata is >600 m (Figs. 3C and 4), which is broadly similar to the stratigraphic thickness observed elsewhere such as the Pequop Mountains to ranges to the east (Zuza et al., 2021b) or the southern Ruby Mountains (Colgan et al., 2010). This indicates that bedding-parallel detachment/attenuation faults did not significantly thin the upper-plate stratigraphy.

First, slip on high-angle normal faults was restored to see the geometric relationships among the upper plate, detachment fault, and lower plate (Fig. 11A). The restored faults are generally high angle with minimal observed fault separation (less than tens of meters). Across our cross-section model, this restoration suggested that these high-angle structures accommodated ~250 m of horizontal extension. This reconstruction shows how the detachment fault is mostly a hanging-wall flat below Diamond Peak, but there are three distinct hanging-wall ramps that cut up to the Pennsylvanian Ely Limestone. There are several high-angle fault splays that root into the detachment fault, which require several hundred meters of displacement in this restoration.

There are poor constraints on where the upper-plate stratigraphy ultimately restores back to, although this location is needed to establish the minimum magnitude of detachment-fault–related displacement (Fig. 11B). Based on conservative, analogous observations from the southern Ruby Mountains (Colgan et al., 2010) and Pequop Mountains to the east (Zuza et al., 2021b), we assume that the detachment-footwall rocks had rotated at least 30° to the east during progressive detachment faulting and later high-angle normal faulting, which implies a steeper original geometry for the detachment fault and adjacent wall rock. Specifically, the thermochronology traverse of Colgan et al. (2010) in the southern Ruby Mountains suggested 40° of eastward footwall tilt driven by westward slip on the detachment fault and western high-angle range-bounding normal-fault system. Both fault systems link from the southern Ruby Mountains to our study area in the East Humboldt Range. Similarly, Zuza et al. (2021b) interpreted that the Pequop Mountains to the east were tilted 30°–40° eastward by westward slip on the western range-bounding normal-fault system. The fault system in the Pequop Mountains is similar to the western range-bounding normal-fault system in the East Humboldt Range (i.e., the Ruby Mountains fault zone; Fig. 1), with both generating >2-km-thick Miocene basins that were exhumed due to progressive stepping of the range-front normal-fault systems. Late Cenozoic basins sediments are thicker on the west side of the East Humboldt Range than the east side (e.g., Ponce et al., 2011), which further supports more slip on the western

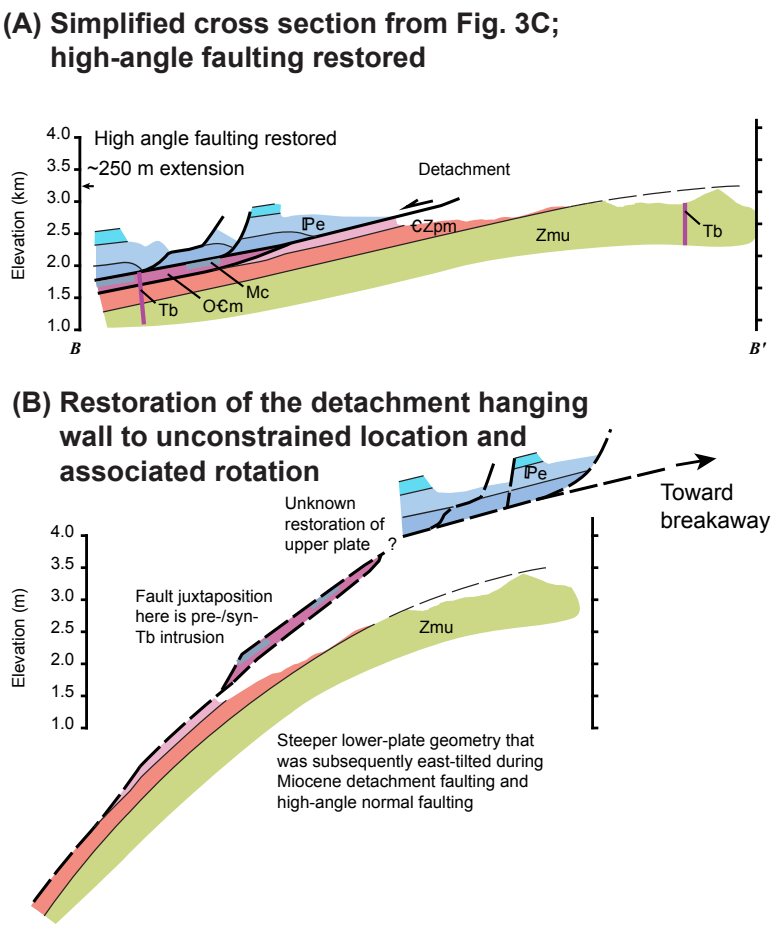

Figure 11. (A) Simplified geologic cross section from the study area, with high-angle normal faults restored (see Fig. 3C for original cross section). (B) Plausible restoration of cross section in A that moves the hanging-wall plate to a higher structural position and tilts the footwall mylonites to an originally steeper west dip. The magnitude of detachment slip is speculative. The moderately strained O€m package is intruded by Tb, similar to underlying €Zpmi-Zmu mylonites, and thus it was juxtaposed against the mylonitic footwall prior to Tb emplacement. Map symbols are defined in Figure 3.

range-bounding normal-fault systems. Pleistocene–Holocene slip rates on both the Pequop Mountains and East Humboldt Range frontal normal-fault systems are similar (0.1–0.2 mm yr^{-1}; Wesnousky and Willoughby, 2003; Zuza et al., 2021b, 2022a). The simplest interpretation is that both ranges were similarly tilted during Basin and Range extension (Zuza et al., 2022a), consistent with most other ranges in the Basin and Range Province (e.g., Stewart, 1980; Colgan et al., 2010, 2020).

The Ruby Mountain–East Humboldt Range detachment-fault system must have a breakaway located to the east. To the southeast, in the southernmost East Humboldt Range, nonmylonitic, non-metamorphosed Upper Paleozoic–Triassic rocks, covered by Eocene volcanic rocks (Brooks et al., 1995), are faulted against metamorphosed but non-migmatitic Ordovician–Devonian rocks (Taylor, 1984). The Ordovician–Devonian rocks have a similar character to those observed in the Wood Hills to the east (e.g., Camilleri, 2010b). The hanging-wall rocks dip eastward into a gently west-dipping fault (Taylor, 1984). If this relationship represents a structurally higher component of the fault system examined in this study, then the corresponding footwall cutoff—and possible breakaway—must be located further east. To the northeast of our study, in the Clover Hill area, Tertiary volcanic rocks are tilted eastward with an ~45° cutoff relationship in the hanging wall (Fig. 2). This observation provides a constraint on the initial geometry and dip of the primary detachment fault or a related splay where it cut and displaced the Miocene volcanic rocks (i.e., originally dipping 45° west). This hanging-wall cutoff also must restore back to an equivalent footwall ramp. This location is not uniquely constrained but may be above the Wood Hills or Pequop Mountains to the east (e.g., Camilleri and Chamberlain, 1997; Zuza et al., 2021b). In the northwest Wood Hills, Upper Paleozoic strata (i.e., Pennsylvanian and Mississippian) and Cenozoic deposits (i.e., Eocene volcanic rocks and Miocene deposits; Brooks et al., 1995) are in normal-fault contact with Ordovician rocks, which may represent an eastward continuation of the detachment-fault system (Thorman, 1962; Camilleri, 2010b). More work is needed to disentangle these relationships, but current observations are broadly compatible with the top-to-the-W normal-fault system deforming structurally higher stratigraphy in the Wood Hills to the east of the East Humboldt Range. Therefore, we speculate that the local breakaway of this detachment-fault system was located above the Wood Hills.

These interpretations allow for a rough estimate of detachment-fault displacement, assuming that the detachment fault involved a west-northwest slip vector, similar to most other Miocene extension in northeast Nevada (e.g., Colgan and Henry, 2009; Zuza et al., 2021a). There must have been at least 16 km of map-view displacement to connect the fault relationships in the southeast East Humboldt Range (Taylor, 1984) with the Tent Mountain map area and ~26 km of displacement to link them with the Wood Hills exposures (Fig. 1; Thorman, 1962; Camilleri, 2010b). A limitation to this approach is that subsequent Basin and Range extension stretched this map-view separation, potentially exaggerating the detachment-fault–related displacement. Colgan et al. (2010) estimated 15–22 km of slip on the Ruby Mountain detachment in the southern Ruby Mountains, which is comparable to our estimates here (16–26 km).

Lower-Plate Ductile Shearing

Here, we focus on Cenozoic deformation that impacted the lower plate beneath the detachment fault, while acknowledging that the earlier phase of Jurassic–Cretaceous shortening strain is poorly constrained. Detailed metamorphic petrology and geochronology studies have revealed the timing and conditions of Jurassic and Cretaceous metamorphism, but the regional interpretations of Mesozoic shortening are enigmatic (Hudec, 1992; Jones, 1999; McGrew et al., 2000; Hallett and Spear, 2014, 2015; Zuza et al., 2020, 2022a). There are some well-documented observations of Mesozoic, possibly Jurassic, thrust-related duplication, such as in the northern Ruby Mountains, where the Ogilvie thrust duplicates Neoproterozoic–early Paleozoic rocks (e.g., Howard et al., 1979; Howard, 1980). The oldest recognized phase of deformation interpreted in this study was observed in Dorsey Creek, where observations of sheared Devonian Guilmette marbles intruded by undeformed Eocene granodiorite require pre–39 Ma deformation (Figs. 8 and 9). There are two possible scenarios for this deformation. First, mylonitic shearing of the Paleozoic marbles may have occurred in the Eocene during an early phase of extension and exhumation. For example, Eocene hornblende $^{40}Ar/^{39}Ar$ ages have been used to suggest early extension and exhumation at this time (McGrew and Snee, 1994) associated with a potentially regionally significant phase of Eocene extension (e.g., Gans et al., 2001; Canada et al., 2019). Alternatively, ductile shearing may have occurred during Jurassic–Cretaceous thrusting when Lower Paleozoic rocks were placed over Mississippian strata, as sketched in Figure 12. The Pequop Mountains provide a useful analog for this model because they record similar thrust juxtaposition (Camilleri and Chamberlain, 1997; Zuza et al., 2020, 2021b), but they were not subsequently overprinted by penetrative Cenozoic normal-sense shearing. In the Pequop Mountains, the Independence thrust places Ordovician rocks over Mississippian Chainman Shale. For most of the exposure of this fault, the wall rock becomes mylonitic with top-to-the-SE shearing within ~100 m of the fault contact (Camilleri and Chamberlain, 1997; Zuza et al., 2021b). Therefore, we argue that this exposure in Dorsey Creek may reflect a similar Mesozoic thrust-fault history. We favor an interpretation of Mesozoic thrusting at this outcrop because it simultaneously explains the pre–ca. 39 Ma timing of shearing and the observed older-over-younger thrust relationships (Fig. 8).

Regardless of the formation mechanism, our observations in Dorsey Creek require a tectonic evolution where less-deformed (to undeformed) Eocene granodiorite (ca. 39 Ma Tgd and Tgo) was juxtaposed via attenuation, ductile excision, or faulting against the mylonitic Lower Paleozoic–Neoproterozoic rocks exposed just to the east in the East Humboldt Range (Fig. 3). Therefore, we propose that most of the rocks in the western Dorsey Creek area occupied a structurally higher position in Eocene to Oligocene time. Eocene granodiorite-monzogranite exposures are relatively rare in the East Humboldt Range, and they differ from the

more widespread and voluminous Eocene quartz diorite (ca. 38–40 Ma Tqd). Eocene granodiorite (Tgd) and granitic orthogneiss (Tgo) are relatively undeformed (Figs. 9B and 9D) compared to the foliated and lineated Eocene quartz diorite (Tqd) (Fig. 9E). Because of the differences between Tqd and Tgd-Tgo, we interpret that Tqd was structurally deeper and deformed during middle–late Oligocene shearing, whereas Tgd-Tgo was structurally higher to mostly avoid such deformation (e.g., Fig. 12). The Eocene granodiorite observed in this study is similar to the internally undeformed Eocene Harrison Pass pluton in the central Ruby Mountains that intruded into non-metamorphosed Paleozoic strata (e.g., Barnes et al., 2001), which confirms that these plutonic bodies may have intruded into relatively high structural levels of the metamorphic core complex. Some combination of Oligocene attenuation and shearing and Miocene detachment faulting juxtaposed the structurally higher blocks consisting of Tgd-Tgo against the deformed lower rocks intruded by Tqd (Fig. 12). This faulting developed the ramp structures observed at Dorsey Creek (Figs. 7A–7E).

The Oligocene top-to-the-W shearing and unit attenuation of the lower plate were systematically described by Zuza et al. (2022a), building on past studies of the area (e.g., Snoke, 1980; Hurlow, 1987; Wright and Snoke, 1993). Briefly, this phase of deformation vertically attenuated the lower-plate Neoproterozoic–Paleozoic stratigraphy and intruding Late Cretaceous–Cenozoic intrusions by >80%. Penetrative fabrics involved top-to-the-W shear kinematics and WNW stretching lineations (e.g., Fig. 3). The deformation of ca. 29 Ma Oligocene granites implies that this deformation occurred in the middle–late Oligocene. The mylonites are crosscut by subvertical ca. 17 Ma basalt dikes, which require mylonitic shearing had ceased by ca. 17 Ma (Table 1). Documented cooling of the lower plate suggests that mylonitic shearing was probably complete by ca. 25–22 Ma, as evidenced by muscovite and biotite $^{40}Ar/^{39}Ar$ dates and overlapping titanite, apatite, and zircon fission-track ages (Table 1; Dallmeyer et al., 1986; Dokka et al., 1986; McGrew and Snee, 1994; Gifford et al., 2008).

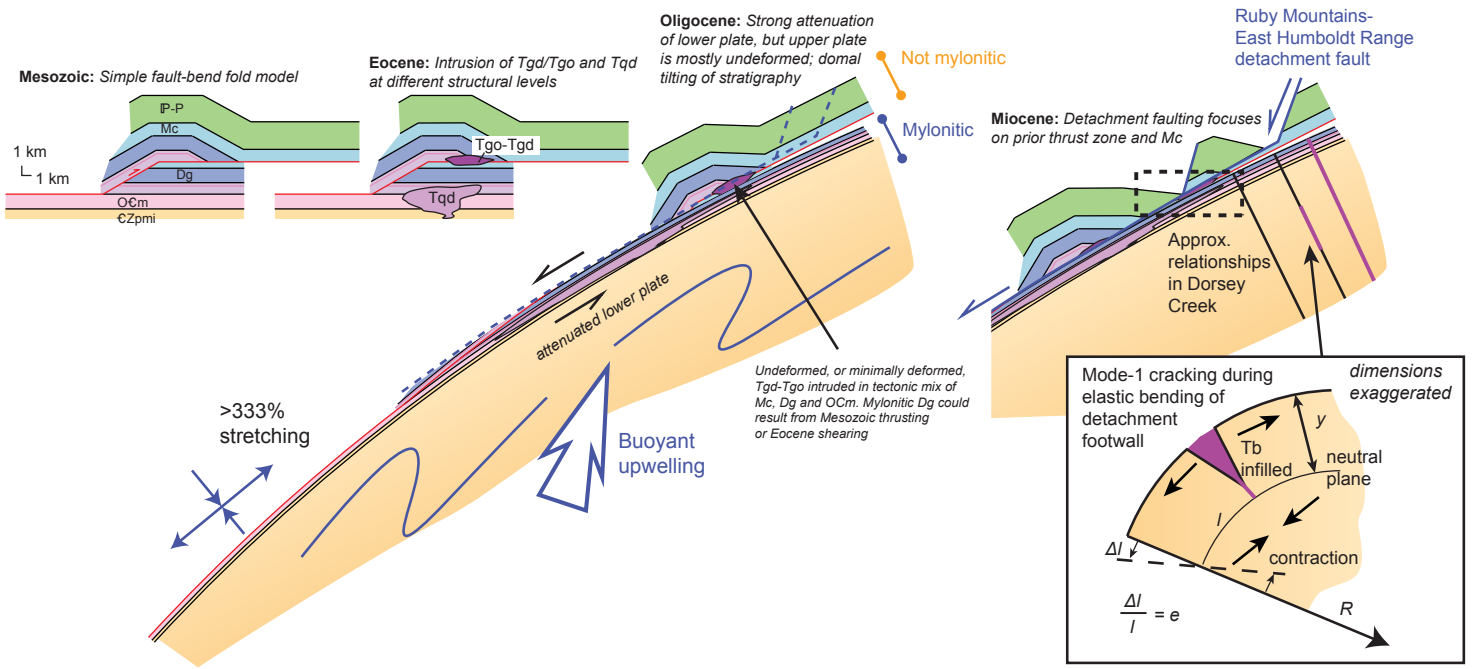

Figure 12. Simple kinematic model to explain juxtaposition relationships observed in the study area. Most igneous rocks are not drafted in this figure, except the distinctly different character of Eocene rocks (e.g., Fig. 9). A Mesozoic fault-bend fold placed Ordovician rocks over Mississippian strata, resulting in local mylonitic shearing near the fault (similar mylonitic shearing and fault offsets are recorded in the Pequop Mountains; Zuza et al., 2021b). Eocene intrusions were emplaced at high (Tgo-Tgd) and lower (Tqd) structural levels. In the Oligocene, the lower part of the structural section was strongly attenuated and sheared, including Tqd intrusions. Stretching of 333% is drafted to equate to 70% attenuation, although these values may be >80%–90% (Zuza et al., 2022a). Oligocene attenuation and later detachment faulting juxtaposed the minimally strained upper plate (with Tgo-Tgd) against the more strongly deformed lower plate. The detachment fault exploited earlier fault zones and Chainman Shale horizons. The detachment footwall developed mode-1 opening cracks and coeval basalt diking (Tb), which can be modeled via simple elastic plate bending. Inset shows setup of variables; see text for description. Map symbols are defined in Figure 3.

Brittle Deformation of the Lower Plate and Detachment Faulting

The aforementioned Oligocene top-to-the-W mylonitic shear zone exposed across much of the bedrock of the East Humboldt Range was crosscut by (1) low-angle detachment faults that were subparallel to the mylonitic fabric, (2) steep brittle tensile fractures, and (3) ca. 17–15 Ma basalt dikes. The basalt dikes intrude the steep fractures, and we interpret that diking and fracturing were approximately synchronous. All dated basalt span 17–15 Ma, with ages from the northwest-striking dikes yielding ca. 17 Ma ages. Therefore, we suggest that this phase of diking and fracturing occurred ca. 17 Ma, which is when Basin and Range extension broadly initiated in the region (e.g., Colgan and Henry, 2009). These basalt dikes were cut by the primary detachment fault, as observed in the Dorsey Creek region, which suggests that the observed exposures of the detachment fault accommodated fault slip after ca. 17 Ma (Table 1). This crosscutting relationship allows detachment slip to have been active prior to ca. 17 Ma, although we note that the correlation between rapid ca. 17 Ma cooling tracked by apatite fission-track and (U-Th)/He thermochronology from the southern Ruby Mountains (Colgan et al., 2010) and the 16 Ma initiation of Humboldt Formation sedimentation strongly suggests that the detachment slip may have initiated synchronous with or just after ca. 17 Ma (Table 1).

Based on these observations, we interpret the following kinematic model. Regional extension initiated at ca. 17 Ma and was accompanied by fast exhumation rates and top-to-the-W detachment faulting at ca. 17–15 Ma, which is recorded by the aforementioned thermochronology from the southern Ruby Mountains (Colgan et al., 2010) ~60 km to the south. Although the Colgan et al. (2010) traverse is significantly south of the study area, it is interpreted that the continuous Ruby Mountains East Humboldt Range were exhumed by the same detachment fault and generated the same mid-Miocene Humboldt Formation basin deposits on the western flanks of this range.

In the study area in the East Humboldt Range, the detachment fault is subparallel to mylonitic fabrics, exhibits a hanging-wall flat–footwall flat geometry, and does not cut significantly down section (i.e., Mississippian rocks are detachment faulted onto Mississippian–Devonian rocks; Figs. 3 and 11). These observations suggest that the detachment fault was focused and concentrated within the Mississippian Chainman Shale, the previous Mesozoic thrust fault, and/or the top of the Oligocene mylonite zone (Fig. 12). This west-directed detachment slip and later high-angle normal faulting would have tilted the footwall blocks eastward, as discussed above. Based on these observations, we interpret that the detachment fault cut and exploited preexisting west-dipping geometry that may have been generated by the Oligocene phase of buoyant doming and mylonitic shearing (Zuza et al., 2022a; Levy et al., 2023). Our reconstruction of Miocene faulting suggests that the western flank of this dome would have dipped ~40°–55° west, and thus Miocene detachment faulting may have initiated at this moderate angle.

Northwest-striking dikes and fractures in the footwall are subvertical today. If we assume that top-to-the-W detachment faulting and high-angle faulting caused eastward rotation of the footwall, then the dikes and fractures would have been formed as east-dipping features. We interpret these formed during brittle detachment faulting, where elastic footwall rocks were stretched and/or flexed (Spencer, 1982, 1985; Gans and Gentry, 2016) to generate north-striking, east-dipping fractures and dike networks. A simple calculation of this follows. Convex bending of an elastic beam will extend above the midplane, y, and contract below it (see inset in Fig. 12). At a distance y from the midplane, the beam will change in length (Δl) from its original l, and the extensional strain, e, of the beam equals y/R, where R is the radius of local curvature (inset of Fig. 12; Turcotte and Schubert, 2002). Elastic crack theory as summarized by Pollard and Segall (1987) provides the relationships between mode-1 crack spacing, S, and vertical crack length, a, in an elastic medium (see eq. 8.52a *in* Pollard and Segall, 1987), herein rearranged to:

$$\frac{S}{a} = \frac{1}{2}\left(\frac{C^{\frac{1}{3}}}{\sqrt{1-C^{\frac{2}{3}}}}\right), \quad (1)$$

where C is the fraction between the yield strength of the rock and the applied remote stress. We assume the crack cuts the extensional part of the bending elastic beam, such that a equals y, and if C is 99%–66%, then $S/a = S/y$ equals ~6 to ~1. Because the fractures are spaced ~500 m apart (Fig. 3A), y is thus ~83–500 m. Assuming the radius of the bending elastic beam is ~10 km (i.e., the length scale across the range), then e is 0.8% to 5%, which equates to 80–500 m of local extension. Mapped fractures and infilled Miocene basalt dikes are ~10–20 m in width (Fig. 5E), and we mapped ~10 parallel structures, including those in the Humboldt Peak quadrangle (McGrew, 2018), which integrates to ~100–200 m of extensional opening. These values demonstrate that Miocene basalt diking and opening fractures in the study area could have been generated by elastic plate bending during detachment faulting. Detachment-fault slip occurred while the lower plate was cold and brittle, which generated fractures in the detachment footwall. This model implies the dikes may have formed with moderate east dips.

Our interpretation that the ca. 15.3 Ma rhyolite was deposited atop the detachment fault north of Dorsey Creek (Figs. 3 and 10) implies that a major phase of detachment faulting and unroofing had occurred by ca. 15.3 Ma. It is unlikely that all of the estimated 16–26 km of detachment slip occurred from ca. 17 Ma to 15.3 Ma, which would equate to unreasonably fast slip rates of ~9–15 mm/yr. For context, thermochronology traverse of Colgan et al. (2010) in the southern Ruby Mountains led to interpreted slip rates of 3–6 mm/yr. However, the involvement of Jarbidge-type rhyolite in the detachment-fault hanging wall near Clover Creek (unit Tr_2 in Fig. 2) suggests that slip on the detachment fault, or a related splay, continued after ca. 15.3 Ma. If the ca. 15.3 Ma rhyolite was indeed deposited on the detachment footwall, we envision that slip continued on different synthetic fault strands during the middle–late Miocene. For example, the eastward tilting of the Clover Creek stratigraphy implies down-to-the-W normal faulting on a normal fault east of the East Humboldt Range. Assuming rapid range exhumation and detachment slip ceased by 12–10 Ma (Colgan et al., 2010), our estimated bulk

slip rates would be more reasonable at 2.3–5.4 mm/yr, which overlap those of Colgan et al. (2010).

High-angle normal faulting and synextensional basin formation continued from the middle Miocene to the present, generating and tilting the Miocene Humboldt Formation. In the study area, strata in the synextensional basin tilted toward the west-dipping normal fault (i.e., the eastern range-bounding normal fault) along the western flank of the East Humboldt Range (Fig. 3; Zuza et al., 2022a).

Implications for Low-Angle Detachment-Fault Generation

The Ruby Mountain–East Humboldt Range detachment fault currently has a shallow (≤10°W) dip (Fig. 3C). Its mapped exposures are consistent with the fault developing at a low angle to hanging-wall and footwall bedding/foliation attitudes, thus appearing as a low-angle normal fault. However, the initiation of and slip on low-angle normal faults are mechanically unfavorable (Axen, 2004; Collettini, 2011). We used observations from our field study to evaluate the mechanical feasibility of our interpreted history of detachment faulting.

The Ruby Mountain–East Humboldt Range detachment exploited weak shaley layers in the Mississippian Chainman Shale. The reactivation of cohesionless preexisting weaknesses follows:

$$\sigma_s = \mu_s(\sigma_n - P_f), \quad (2)$$

where σ_s is shear stress, σ_n is normal stress, P_f is pore-fluid pressure, and μ_s is the coefficient of sliding friction. Byerlee (1978) showed that for most rock types, μ_s equals 0.85 for σ_n < 200 MPa. Following Collettini and Sibson (2001), we rewrite Equation 2 in terms of principal stresses (maximum and minimum principal stresses, σ_1 and σ_3, respectively), normalized for vertical stress, σ_v, as the frictional reactivation parameter, Γ:

$$\Gamma = \frac{(\sigma_1 - \sigma_3)}{(\sigma_v - P_f)} = \frac{\mu_s(\tan\alpha + \cot\alpha)}{(1 + \mu_s \cot\alpha)}, \quad (3)$$

where α is the angle between σ_1 and the failure plane. In Mohr notation, θ is the angle between a vector normal to the failure plane and σ_1, such that $\theta + \alpha = 90°$. For regional extension, $\sigma_v = \sigma_1$, and thus α equals the inferred dip of a failure plane (Fig. 13A). Faulting is favored at orientations that minimize the frictional reactivation parameter, and thus Γ minima for μ_s values of 0.85, 0.6, and 0.4 predict fault dips of 65°, 60°, or 56°, respectively (Fig. 13B).

To explore the development of the apparently low-angle Ruby Mountain–East Humboldt Range detachment fault, we require integration of the geologic history. Peak rock strength (differential stress, $\sigma_1 - \sigma_3$) near the brittle-ductile transition is ~150 MPa (Behr and Platt, 2011, 2014; Zuza et al., 2022a, 2022b). We envision the nascent detachment in the Mississippian Chainman Shale would have formed at a structural depth of ~6 km, based on its original stratigraphic depth and potential thrust duplication discussed in this work. Therefore, we linearly scale the peak strength of 136 MPa at ~10 km depth estimated by Behr and Platt (2011) to get peak strength of 82 MPa at ~6 km depth. We assume $\sigma_v = \sigma_1$ = ~150 MPa, based on ~5–6 km depth and lithostatic pressures. Similar magnitudes of middle Miocene range exhumation detachment faulting and range rotation have been documented in the southern Ruby Mountains (Colgan et al., 2010) and Pequop Mountains (Zuza et al., 2021b).

With this configuration, the rock does not intercept the Byerlee sliding envelope ($\sigma_s = 0.85\sigma_n$; Fig. 13C). However, two additional observations refine our setup. Observed quartz veining within the Chainman Shale–dominated detachment-fault breccia zone implies substantial pore-fluid pressure (Fig. 5D). The detachment fault is primarily located within the Chainman Shale, and there are no observations of low-angle klippe exploiting other fault planes. That is, all observed hanging-wall motion involves Mississippian Diamond Peak Formation, which is consistent with faulting in the Chainman Shale that stratigraphically underlies the Diamond Peak Formation. We infer that most of the other rock types were stable, except unique low-friction shaley horizons. The Mohr circle intersects the Byerlee sliding envelope with less-than-hydrostatic pore-fluid-factor (λ) conditions of λ = 0.30 (Fig. 13C), which is reasonable compared to other detachment-fault systems (e.g., Axen, 1992; Axen and Selverstone, 1994; Behr and Platt, 2011). With slip concentrated in the shale rocks or previous fault horizons, we also show a sliding envelope with a weaker μ_s of 0.4 (e.g., Numelin et al., 2007; Kohli and Zoback, 2013), which leads to θ = 26° (Fig. 13C).

This analysis suggests that cohesionless, low-friction shale layers could have been reactivated for normal faulting at dips of ~30°, whereas the rest of the rock remained relatively stable. This dip is relatively low for a normal fault but still greater than subhorizontal, as might be implied from hanging-wall flat–footwall flat fault relationships in undeformed and nontilted strata. Our reconstruction for the initial predetachment configuration suggests a moderate dip of ~40° west or greater. The observed ~45° cutoff relationship in the Clover Creek area (Fig. 2) is consistent with the detachment fault originating with these moderate dips. Although the predetachment geometry has significant uncertainty, it most likely had moderate initial dips. Furthermore, almost every range in the eastern Great Basin has been tilted by Miocene–present extension (e.g., Stewart, 1980), and therefore the subhorizontal shallow dips in the East Humboldt Range today were most likely steeper prior to the Miocene. Greater μ_s values imply steeper failure planes >30°.

In this regard, we argue that the pre–middle Miocene structural and geometric configuration was readily reactivated by normal faulting. More specifically, our interpretations indicate that Oligocene upwelling and doming (Zuza et al., 2022a; Levy et al., 2023) established a favorable orientation for the mechanically weak Chainman Shale and Mesozoic thrust faulting along the dipping flanks of the dome to be exploited by Miocene detachment faulting (Figs. 13D and 13E). The low-angle geometry of the fault is only apparent because it was focused in the shaley horizons and was subsequently rotated eastward during detachment faulting and later high-angle faulting. In the Pequop Mountains, two ranges east of the East Humboldt Range (Fig. 1), the Pequop low-angle normal fault has a similar interpreted evolution. Mesozoic thrust faulting along the Independence thrust led to a moderate-steepness, west-dipping back limb (30°–40°), and later Cenozoic (probably

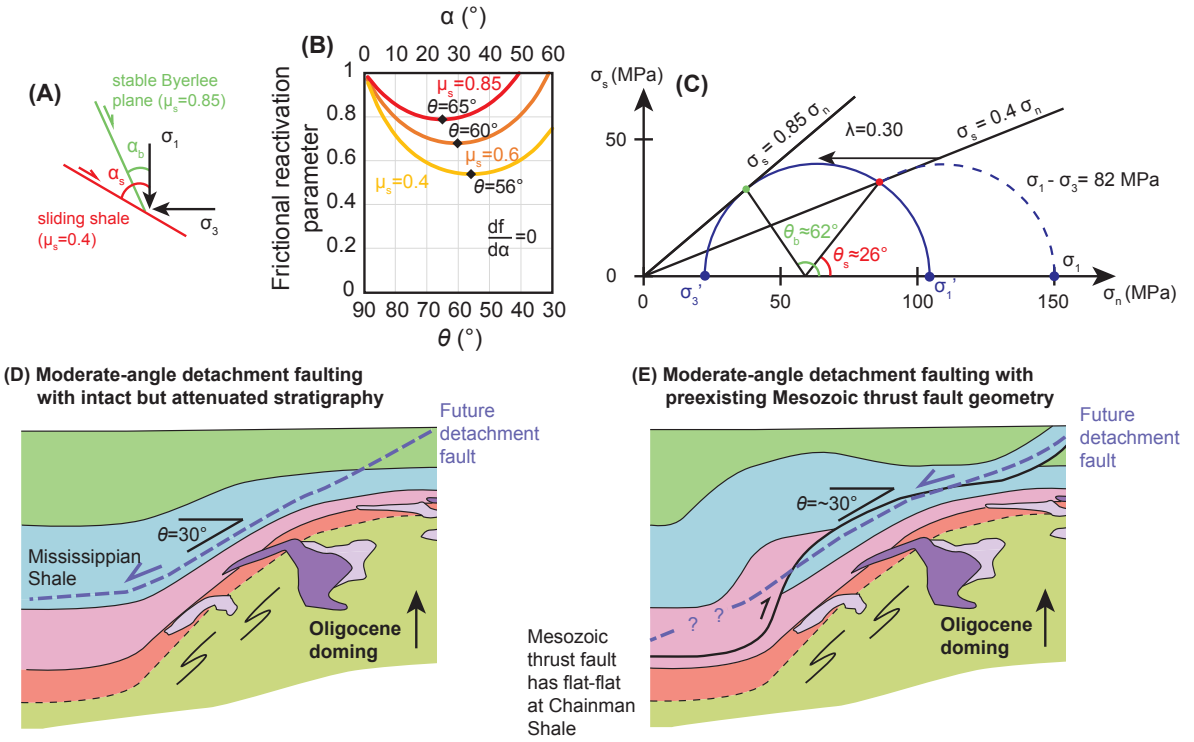

Figure 13. (A) Setup of variables, assuming a simple normal-fault geometry, a predicted Byerlee failure plane, and a weak sliding shale horizon. (B) Frictional reactivation parameters for different frictional sliding parameters (μ_s) plotted as a function of fault dip, θ (e.g., Collettini and Sibson, 2001). See text for equations. Curve minimums shows the geometries that are most readily reactivated. (C) Mohr circle explanation for low-angle faulting in the East Humboldt Range. Hydrostatic pore-fluid pressure pushes the Mohr circle toward the Byerlee frictional sliding curve, but because most bedrock is undeformed, we assume the rock does not intercept this envelope. Instead, shaley horizons with lower friction (μ_s = 0.4) are reactivated, leading to a fault dip of ~29°. (D–E) Miocene reactivation of relatively weak horizons, following Oligocene doming, is possible if the detachment fault was focused in (D) the Mississippian Chainman Shale (Mc) or (E) a combination of Mc and the preexisting thrust-fault geometry with clay-rich gouge. In either case, footwall rebound would lead to eastward rotation to a subhorizontal geometry.

middle Miocene) normal faulting exploited this back-limb geometry to develop an apparent low-angle normal fault (Fig. 14; Zuza et al., 2021b). Although some reconstructions favor a Late Cretaceous age for the Pequop fault (e.g., Camilleri and Chamberlain, 1997), we prefer a Miocene age for detachment faulting in the Pequop Mountains (e.g., Zuza et al., 2021b) because of (1) the deposition of Eocene volcanic rocks on Middle–Upper Paleozoic rocks near the Pequop fault, which implies limited deep exhumation prior to the Eocene; (2) the lack of pre-Miocene synkinematic deposits, which would be expected for significant pre-Miocene detachment slip; and (3) the simplest assumption that major WNW-directed detachment slip occurred at the same time as detachment faulting in the East Humboldt Range, which we have argued occurred in the middle Miocene. Accordingly, normal-sense Pequop fault reactivation of a cohesionless surface dipping 30°–40° is viable with hydrostatic pore-fluid pressure and low friction.

These two cases demonstrate that for the Ruby Mountains–East Humboldt Range, the apparent low-angle detachment faulting may be explained by reactivation of moderate-steepness weak zones and subsequent footwall rotation to subhorizontal geometries (Fig. 14). In these cases, the preexisting geometries were generated by either Mesozoic shortening (Pequop Mountains) or Oligocene domal upwarping (East Humboldt Range). Although this explanation cannot explain all instances of low-angle normal faulting (e.g., Collettini, 2011), it emphasizes the role of preexisting crustal heterogeneities in developing apparent low-angle normal faults. Our interpreted evolution requires aspects of the "rolling hinge" (Wernicke and Axen, 1988; Buck,

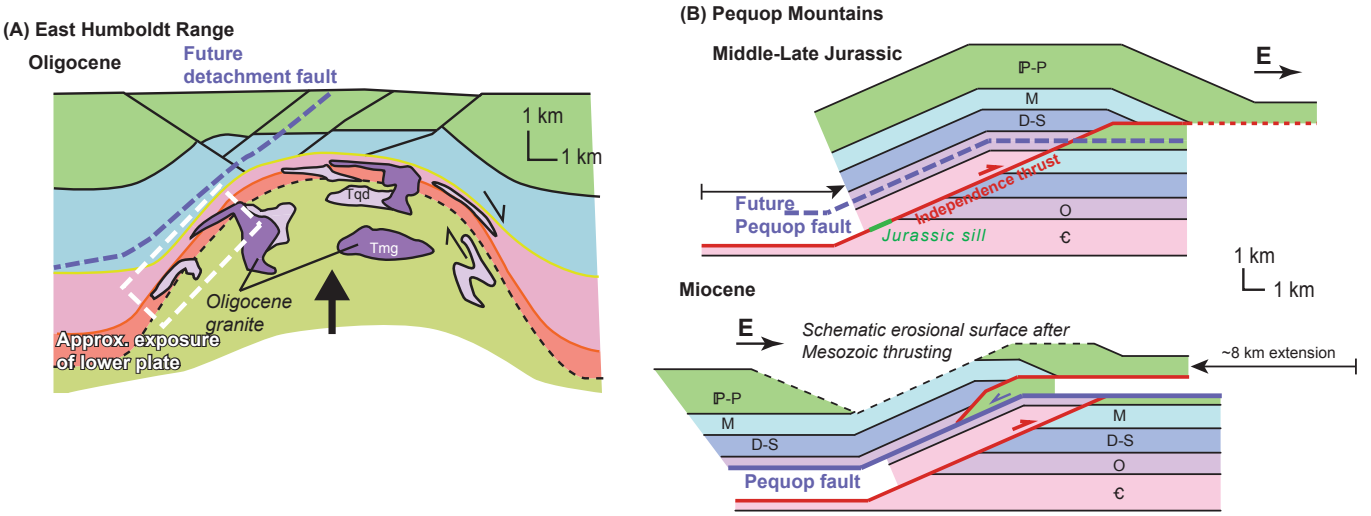

Figure 14. Examples of apparent low-angle normal faults in northeast Nevada, including (A) the Miocene Ruby Mountains–East Humboldt Range detachment fault (this study; Zuza et al., 2022a) and (B) the Pequop normal fault, of probable Miocene age (Zuza et al., 2021b), in the Pequop Mountains, which reactivates the back limb of the Jurassic Independence thrust (Camilleri, 2010a; Zuza et al., 2021b). P—Pennsylvanian-Permian; M—Mississippian; D-S—Devonian-Silurian; O—Ordovician; Є—Cambrian.

1988) or block-rotation (Wong and Gans, 2008) models, where brittle faults were initiated at moderate dips and subsequently were rotated to shallower geometries. This fault rotation may be caused by isostatic rebound of the footwall rocks during progressive hanging-wall removal, and evidence for this hanging-wall removal includes synkinematic basin sedimentation (e.g., Lund Snee et al., 2016).

Our interpretations do not preclude the general existence of low-angle normal faults, but our findings from northeast Nevada suggest that apparent low-angle fault slip was influenced by preexisting geometries. There are regions where active, low-angle slip has been observed (Wernicke, 1995; Axen, 1999; Kapp et al., 2008), which supports their existence in other geologic settings. However, there are also examples where careful reevaluation or subsequent analysis suggested that high-angle faults are the dominant active structures compared to nearby, low-angle structures (Gold et al., 2020), including our interpretations that high-angle faults presently cut the Ruby Mountain–East Humboldt Range detachment fault.

Metamorphic Core Complex Domes Preconditioned Miocene Detachment Faulting

Metamorphic core complexes and detachment faults in the North American Cordillera define a belt stretching from Canada to Mexico (e.g., Coney, 1980; Whitney et al., 2013) that spatially overlaps the two-mica peraluminous Cretaceous–Paleogene plutonic belt (e.g., Miller and Bradfish, 1980). This spatial correspondence may imply, but does not require, a causal relationship between processes of peraluminous plutonism and metamorphic core complex generation, which both occurred well before late Cenozoic extension initiated across western North America. Indeed, the parallelism between these features and the western plate boundary and (paleo-) subduction zone suggests that subduction processes and Farallon slab dynamics played a first-order role in this geologic history.

First, we discuss the geologic events that impacted northeast Nevada in relation to the development and evolution of metamorphic core complexes and Basin and Range extension (Fig. 15). In the Cretaceous, the crust was relatively thick in this region (~60 km) as part of the hypothesized Nevadaplano orogenic plateau (DeCelles, 2004; Zuza et al., 2021b). In the Late Cretaceous, the east-dipping Farallon slab started to shallow, culminating in early Cenozoic flat-slab subduction and the Laramide orogeny (e.g., Bird, 1984; Copeland et al., 2017). This slab shallowing occurred at the same time as the emplacement of the peraluminous pluton belt in North America, which has debated origins (Fig. 15; see recent review by Chapman et al., 2021). Post-Laramide slab rollback led to asthenospheric upwelling and coupled volcanism that swept southwest from Idaho latitudes to southern Nevada during the Eocene through Miocene (e.g., Copeland et al., 2017; Zuza and Cao, 2023). The volcanic rocks filled in paleovalleys that would have been carved into the high-elevation orogenic plateau (Henry, 2008).

Eocene rollback volcanism generated mantle-derived intermediate-mafic intrusions in the East Humboldt Range, which were subsequently

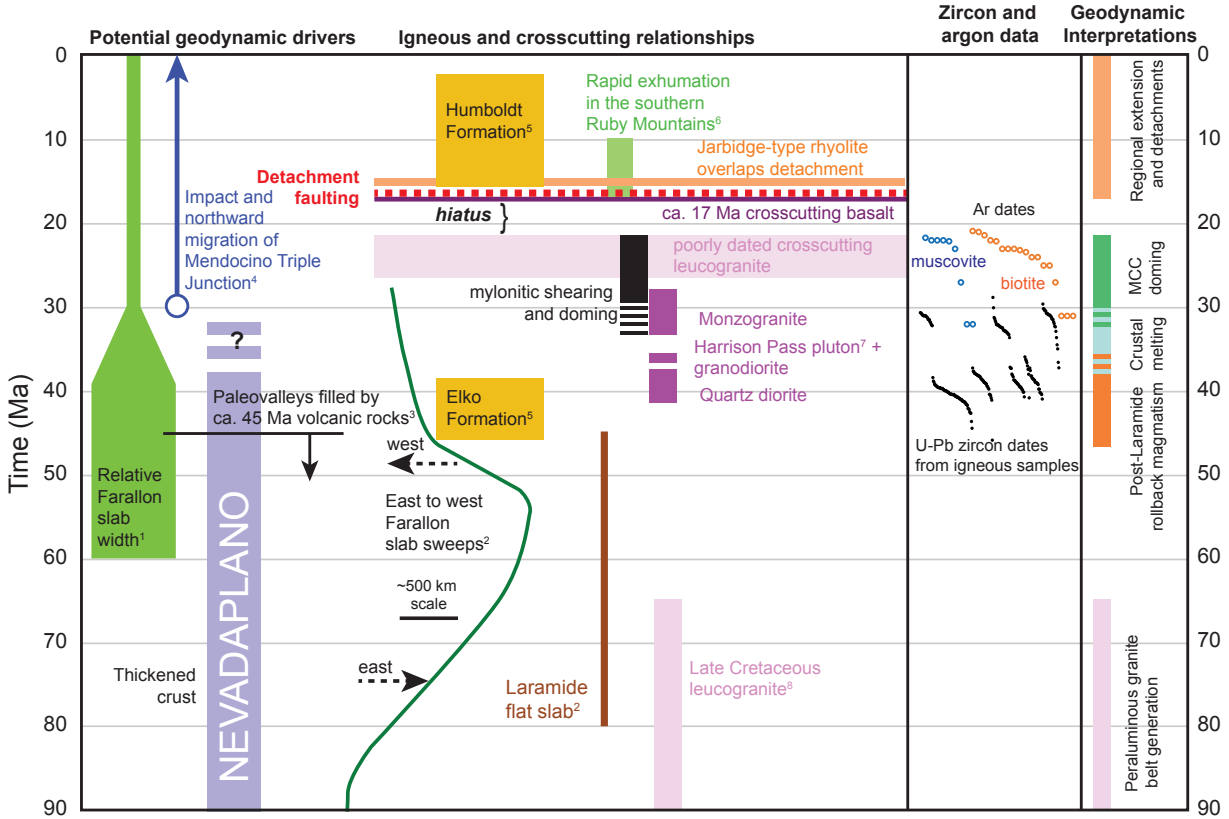

Data sources: (1) Schellart et al. (2010); (2) Copeland et al. (2017); (3) Henry (2008); (4) Clennett et al. (2020), Zuza and Cao (2023); (5) Smith et al. (2017), Lund Snee et al. (2016); (6) Colgan et al. (2010); (7) Barnes et al. (2001); (8) Howard et al. (2011); and this study and other references discussed in the text.

Figure 15. Tectonic summary diagram for major regional events that impacted the geology in northeast Nevada. Data sources are listed in the figure. Argon muscovite and biotite dates are summarized in Table S2 (see text footnote 1). Individual zircon spot ages are from this study and Zuza et al. (2022a). See text for discussion. MCC—metamorphic core complex.

intruded by Oligocene granites and leucogranites that probably reflect remelting of the mid- and lower crust (Howard et al., 2011). Mylonitic shearing deformed the Eocene–Oligocene granites in the East Humboldt Range during the primary metamorphic core complex phase of deformation (e.g., Wright and Snoke, 1993; Zuza et al., 2022a). Fission-track and argon thermochronology data sets suggest that the shear zones cooled below ~300 °C by ca. 22 Ma (Fig. 15; Dallmeyer et al., 1986; Dokka et al., 1986; McGrew and Snee, 1994; Gifford et al., 2008). The chilled margins and 17 Ma plagioclase $^{40}Ar/^{39}Ar$ dates from basalt dikes (Zuza et al., 2021a) that crosscut the mylonites further demonstrate that the mylonitic shear zone was cold by the middle Miocene. Following an apparent hiatus, regional extension impacted the area (Colgan and Henry, 2009; Colgan et al., 2010) as evidenced by post–17 Ma detachment faulting and the deposition of the Humboldt Formation.

There are several possible mechanisms for Oligocene metamorphic core complex generation, including high-magnitude regional extension or thermally driven buoyant upwelling of the midcrust following post-Laramide rollback volcanism and heating (Konstantinou et al., 2013; Howlett et al., 2021; Zuza et al., 2022a; Levy et al., 2023). If large-scale crustal extension did occur in the Oligocene, it may have been driven by gravitational collapse of the thickened orogenic plateau (e.g., Sonder and

Jones, 1999; Jones et al., 1998) or a pronounced narrowing of the width of the subducting Farallon slab that influenced the continental interior (Schellart et al., 2010). However, regional extension at this time preceded the main phase of extension driven by plate-boundary conditions and the northward-migrating Mendocino triple junction (Colgan and Henry, 2009). We rule out gravitational collapse as a dominant driver because the Oligocene metamorphic core complex developed 40+ m.y. after peak Late Cretaceous crustal thickening, and we interpret that this region did not experience regional Oligocene extension, as evidenced by the lack of either Oligocene synkinematic basin deposits or observed surface-breaking normal faults. We acknowledge that increased gravitational potential energy may have been an important precursor condition to facilitate buoyant Oligocene doming and Miocene regional extension, but the attainment of some critical crustal thickness did not uniquely drive regional extension without some other external driver (e.g., Gottardi et al., 2020), such as changing plate-boundary conditions.

Our observations of locally unique, voluminous Oligocene pre- or synkinematic intrusions in the East Humboldt Range footwall suggest that magmatism was important for their generation. Furthermore, Oligocene mylonitic shearing without synkinematic basins or any record of substantial paleosurface relief supports an interpretation of passive midcrust upwelling without surface-breaking normal faults. Therefore, we interpret that the East Humboldt Range metamorphic core complex developed predominately as a buoyant dome following Eocene–Oligocene magmatism (Zuza et al., 2022a; Levy et al., 2023). Miocene extension started later as the plate-boundary kinematics drove northwest-directed crustal extension while the Mendocino triple junction migrated northward (e.g., Colgan and Henry, 2009; Zuza and Cao, 2023).

Our model implies that the top and eastern sides of the Oligocene buoyant dome, with potentially antithetic top-to-the-E shear zones, are buried in Clover Valley due to the eastward tilting of the East Humboldt Range. Across the Ruby Mountains–East Humboldt Range, there are areas that were structurally below the mylonitic shear zone, such as the eastern flank of the East Humboldt Range (McGrew, 2018) or northern Ruby Mountains (MacCready et al., 1997), and areas that were clearly always structurally above or adjacent to the Oligocene shear zone, such as the southern Ruby Mountains (e.g., Colgan et al., 2010). This requires some transitional shear zone between the structurally higher, undeformed rocks and the migmatitic lower-plate rocks—i.e., the superstructure versus infrastructure (Armstrong and Hansen, 1966)—that must cross the central Ruby Mountains. There are sparse observations of top-to-the-E fabrics in the central Ruby Mountains (e.g., Hudec, 1992), which could be part of this transitional zone, but more detailed kinematic and timing analysis is required. The inward-facing recumbent fold nappes that trend the length of the Ruby Mountains (e.g., Howard, 1980; MacCready et al., 1997; Snoke et al., 1997, 2022) hint at symmetry across the Ruby Mountains and suggest a mobile flowing midcrust that may have been a part of a growing dome. The doming model may be expected to result in more vertical fabrics associated with vertical flow, which are not observed. We speculate this may be because the finite strain history only records final flattening against the margins of the rising dome or otherwise overprints any vertical flow fabrics (e.g., Kruckenberg et al., 2008, 2011).

We can gain more insight by comparing the East Humboldt Range metamorphic core complex to other similar metamorphic core complex systems in the central North American Cordillera, such as the Albion–Raft River–Grouse Creek metamorphic core complex system to the north and the northern Snake Range to the south (Figs. 1 and 16). The post-Laramide slab-rollback volcanic sweep resulted in volcanism from ca. 44 Ma near the Albion–Raft River–Grouse Creek in the north to ca. 36 Ma in south near the northern Snake Range. Subsequent ductile attenuation, synkinematic intrusions, domal upwelling, and mylonitic shearing are constrained to ca. 32–25 Ma in the Albion–Raft River–Grouse Creek metamorphic core complex (Egger et al., 2003; Strickland, 2010; Strickland et al., 2011a, 2011b; Konstantinou et al., 2013), ca. 29–23 Ma in the East Humboldt Range–Ruby Mountains (Wright and Snoke, 1993; Zuza et al., 2022a), and ca. 38–22 Ma in the northern Snake Range (Lee et al., 2017). A compilation of muscovite and biotite $^{40}Ar/^{39}Ar$ ages constrains the ages of mylonitic shearing and allows for inter–metamorphic core complex comparisons (Fig. 16B; Zuza and Cao, 2023). Although these age ranges broadly overlap, based on the nearly parallel southward-younging trend of preceding volcanism, we interpret that ductile shearing during metamorphic core complex generation also became younger southward, following the southward-younging trends of rollback volcanism. In this case, each location experienced mylonitic shearing ~10 m.y. after the arrival of rollback volcanism (e.g., Howlett et al., 2021; Zuza and Cao, 2023).

Our favored interpretation for metamorphic core complex generation in the central North American Cordillera is that significant crustal heating driven by slab-rollback magmatism led to buoyant doming of a melt-rich middle crust (e.g., Howard, 1980; Konstantinou et al., 2013; Zuza et al., 2022a; Levy et al., 2023; Zuza and Cao, 2023). Our interpretation explains the severe attenuation of the lower-plate units, timing trends between southward-younging slab-rollback volcanism and metamorphic core complex generation, significant volume of intrusions and crustal melts in the core of some of the metamorphic core complexes, and lack of surface relief or significant basin formation during the main stage of ductile shearing (e.g., Zuza et al., 2022a; Levy et al., 2023; Zuza and Cao, 2023). Although the interpretation of other metamorphic core complexes is beyond the scope of this present study, we speculate this process was important for other metamorphic core complexes in the central North American Cordillera, which explains their similar magmatic and kinematic histories (e.g., Konstantinou et al., 2012, 2013; Zuza and Cao, 2023).

Based on reported timing constraints, there was an apparent hiatus between metamorphic core complex exhumation with mylonitic shearing and later Basin and Range extension. In the Albion–Raft River–Grouse Creek metamorphic core complex, Basin and Range extension and detachment faulting initiated at ca. 14 Ma, ~10–12 m.y. after metamorphic core complex exhumation (e.g., Konstantinou et al., 2012, 2013). As discussed in this work, there was a hiatus between ca. 29–22 Ma metamorphic core complex development and ca. 17–15 Ma Miocene detachment faulting

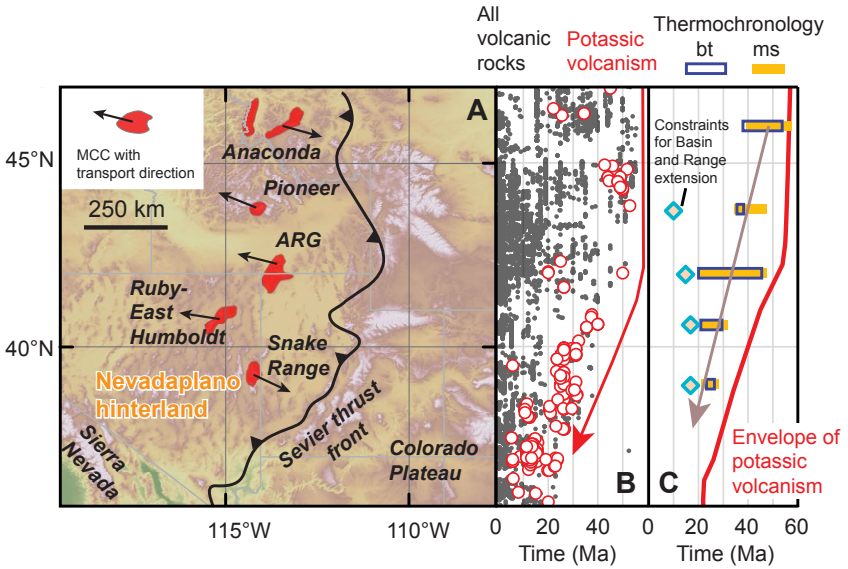

Figure 16. (A) Map showing the location of metamorphic core complexes (MCC) in the Sevier hinterland, including their transport direction. ARG—Albion–Raft River–Grouse Creek metamorphic core complex. (B) Plot of volcanic rocks from the NAVDAT database (https://www.navdat.org/) and potassic volcanic rocks, which shows the southward magmatic sweep that accompanied post-Laramide slab rollback. (C) Biotite (bt) and muscovite (ms) $^{40}Ar/^{39}Ar$ ages for each metamorphic core complex, which broadly track the southward trend of mylonitic shearing and exhumation through the temperature of quartz plasticity. Diamonds show published constraints for the onset of Basin and Range extension, which is broadly ca. 17 Ma or slightly younger (e.g., Miller et al., 1999; Colgan and Henry, 2009; Colgan et al., 2010; Konstantinou et al., 2012, 2013). Note the parallelism between trends in panels B and C, except Basin and Range extension, which migrates northward with the Mendocino triple junction. Figure is modified from Zuza and Cao (2023).

in the East Humboldt Range (e.g., Fig. 15). In the Snake Range, there is a >5 m.y. hiatus between a ca. 22.5 Ma dike that crosscuts the mylonitic shear zone (Lee et al., 2017) and interpreted ca. 17 Ma rapid exhumation and detachment faulting during Miocene–present Basin and Range extension (Miller et al., 1999).

Taken together, we speculate that these three metamorphic core complexes with similar geologic histories formed via post-Laramide magmatism and Paleogene intrusion-related doming. This process would have generated a pervasive crustal-scale fabric that was readily reactivated by later Miocene detachment faulting during regional extension (Colgan and Henry, 2009). This may have formed as a geometric or mechanical preexisting weak zone (e.g., Davis, 2013) that was favorably oriented to concentrate slip on weak stratigraphic or structural horizons. It may have also developed as a thermal and rheological weakness, where the Oligocene upwelling of mass and heat led to local hot and weak anomalies that particularly concentrated Miocene strain in the form of rapid detachment-focused extension. Miocene faulting subsequently exhumed the Oligocene domal structures, which were temporally decoupled from, and later reactivated as, Miocene detachment faults. Miocene detachment-fault slip may have been relatively minor, consistent with the observation of little or no unit omission along the detachment faults (e.g., Miller et al., 1983). Our estimates of ~16–26 km of detachment fault–related slip are on the lower end of typical low-angle normal-fault models for metamorphic core complexes (e.g., Bartley and Wernicke, 1984). Given that the East Humboldt Range exposes some of the deepest, oldest rocks in the Great Basin (e.g., Lush et al., 1988; Premo et al., 2008), these relatively lower estimates of detachment-fault slip emphasize the significance of predetachment Oligocene buoyant doming for lower-plate exhumation. It is possible that most of the Miocene exhumation was accommodated by high-angle normal faulting and subsequent range rotation, similar to much of the eastern Basin and Range (e.g., Colgan et al., 2010, 2020).

Taking an average of ~20 km of slip on the Ruby Mountain–East Humboldt Range detachment-fault system (Colgan et al., 2010; this study), a 45° ± 5° fault dip equates to 13–15 km of horizontal extension. Given that the present-day width of the structural footprint (i.e., the range and structurally adjacent basins) of the East Humboldt Range and Ruby Mountains is ~30–50 km (Fig. 1), these extension magnitudes imply ~35%–100% extension (i.e., 13–15 km horizontal extension divided by a restored width of 15–37 km). The region has a present-day crustal thickness of ~30–35 km (Gilbert, 2012), and assuming pure-shear stretching of the crustal column, the pre-extensional crustal thickness would have been 40–70 km. There are substantial uncertainties in these estimates and this restoration approach (e.g., Say and Zuza, 2021), but they demonstrate that mid-Miocene-to-present extension could have thinned the Mesozoic orogenic plateau from ~60 km thickness (e.g., DeCelles, 2004; Chapman et al., 2015) to present-day values.

Although our interpretations may not apply to all North American metamorphic core complexes, there is growing evidence that other metamorphic core complexes developed, or were initiated, during intrusion-related deformation and high heat flux (e.g., Miller et al., 1983; Konstantinou et al., 2012, 2013; Ducea et al., 2020). Careful analysis is needed to explore the extent to which ductile deformation is related to, decoupled from, or a precondition of later Miocene detachment faulting in the development of metamorphic core complexes.

CONCLUSIONS

Here, we provided new field observations, structural reconstructions, and U-Pb zircon dating that constrain the timing and kinematics of Cenozoic deformation within the Ruby Mountains–East Humboldt Range metamorphic core complex. This work led to the following primary conclusions:

(1) Records of Mesozoic crustal shortening are cryptic but include older-over-younger fault relationships, which may have been associated with shear fabrics that were subsequently intruded by undeformed Eocene granodiorite. It is also possible that some of these observations reflect Eocene shearing associated with an early phase of extension or complex middle–late Cenozoic folding and shearing that led to apparent thrust-fault relationships. However, based on map relationships and the regional geologic history, we interpret the observed older-over-younger relationships to reflect Mesozoic shortening and thrust duplication, similar to that in adjacent ranges, such as the Pequop Mountains to the east.

(2) The primary phase of top-to-the-W mylonitic shearing deformed Oligocene plutons (ca. 31–29 Ma) and older rocks and thus is interpreted to have occurred in the middle–late Oligocene (e.g., Wright and Snoke, 1993). The episode attenuated Neoproterozoic to middle Paleozoic stratigraphy, juxtaposing less-strained sections, such as less-deformed Eocene intrusions, against strongly deformed rocks. We interpret that the present-day exposures of the mylonitic shear zone represent the tilted western flank of an elongate dome that was generated due to Eocene–Oligocene magmatism, crustal heating, and buoyant upwelling of the middle to lower crust.

(3) The mylonitic shear zone was crosscut by ca. 17 Ma basalt dikes during the middle Miocene initiation of regional extension and detachment faulting. Therefore, the Ruby Mountain–East Humboldt Range detachment faults that place Mississippian strata on the mylonitic rocks were temporally decoupled from the earlier Oligocene mylonitic shear zone. The detachment fault cuts the ca. 17 Ma basalt and appears to have focused in Chainman Shale and preexisting thrust structures. Our reconstruction suggests that the detachment fault may have initiated in a preexisting west-dipping structural geometry developed by earlier Oligocene doming, such that the Miocene faults initiated at moderate dips (~40°–55° west). Detachment faulting and later high-angle normal faulting tilted the entire range eastward. Total detachment slip was >16 km and probably closer to ~26 km, based on mapped exposures of the hanging-wall rocks and estimates for a local breakaway position above the Wood Hills. This displacement range overlaps values estimated for the southern Ruby Mountains (Colgan et al., 2010), which were part of the same broad system.

(4) Our kinematic model for detachment faulting provides a mechanically viable solution for the apparent low-angle normal fault, hanging-wall flat–footwall flat geometry. That is, the detachment fault exploited moderately dipping shaley or fault gouge–rich horizons, with elevated pore-fluid pressure.

(5) Our observations are similar to those in other metamorphic core complexes to the north and south (i.e., the Albion–Raft River–Grouse Creek metamorphic core complex and Snake Range), where Oligocene mylonitic shearing followed Eocene–Oligocene magmatism. An ~10 m.y. delay between mylonitic shearing and later Miocene detachment supports interpretations that (a) the mylonites are not reflective of an early phase of regional extension but rather buoyant doming, (b) the detachment faults initiated with the onset of regional extension, and, thus, (c) the mylonites are not the downdip ductile shear zone part of the detachment faults. This model emphasizes buoyant doming and stretching across the north-south axis of the North America Cordillera, which established favorable rheologic or geometric conditions for focusing detachment faulting along planes of weakness during the onset of Basin and Range extension. Furthermore, our work reiterates that the Cenozoic mylonitic shear zones are not uniquely indicative of regional extension.

ACKNOWLEDGMENTS

This research was supported by the U.S. Geological Survey National Cooperative Geologic Mapping Program via STATEMAP awards (G19AC00383, G20AS00006) and the National Science Foundation Tectonics program (EAR 1830139). We thank Art Snoke and Keith Howard for showing us the geology of the East Humboldt Range, aiding our geologic mapping, and reviewing some of the important unanswered questions. Chuck Thorman, Chris Henry, Al McGrew, and Drew Levy are thanked for thoughtful discussions on the geology of northeast Nevada. Thomas Hoisch provided helpful suggestions on a previous version of this manuscript. Helpful review comments by Science Editor Christopher J. Spencer, Associate Editor Jason W. Ricketts, and four anonymous reviewers greatly improved this manuscript. Joel DesOrmeau assisted with U-Pb dating and Drew Levy made an original version of Figure 1.

REFERENCES CITED

Armstrong, R.L., 1972, Low-angle (denudation) faults, hinterland of the Sevier orogenic belt, eastern Nevada and western Utah: Geological Society of America Bulletin, v. 83, p. 1729–1754, https://doi.org/10.1130/0016-7606(1972)83[1729:LDFHOT]2.0.CO;2.

Armstrong, R.L., and Hansen, E., 1966, Cordilleran infrastructure in the eastern Great Basin: American Journal of Science, v. 264, no. 2, p. 112–127, https://doi.org/10.2475/ajs.264.2.112.

Axen, G.J., 1992, Pore pressure, stress increase, and fault weakening in low-angle normal faulting: Journal of Geophysical Research: Solid Earth, v. 97, no. B6, p. 8979–8991, https://doi.org/10.1029/92JB00517.

Axen, G.J., 1999, Low-angle normal fault earthquakes and triggering: Geophysical Research Letters, v. 26, p. 3693–3696, https://doi.org/10.1029/1999GL005405.

Axen, G.J., 2004, 3. Mechanics of low-angle normal faults, *in* Karner, G., et al., eds., Rheology and Deformation of the Lithosphere at Continental Margins: New York, Columbia University Press, p. 46–91, https://doi.org/10.7312/karn12738-004.

Axen, G.J., and Selverstone, J., 1994, Stress state and fluid-pressure level along the Whipple detachment fault, California: Geology, v. 22, no. 9, p. 835–838, https://doi.org/10.1130/0091-7613(1994)022<0835:SSAFPL>2.3.CO;2.

Barnes, C.G., Burton, B.R., Burling, T.C., Wright, J.E., and Karlsson, H.R., 2001, Petrology and geochemistry of the late Eocene Harrison Pass pluton, Ruby Mountains core complex, northeastern Nevada: Journal of Petrology, v. 42, p. 901–929, https://doi.org/10.1093/petrology/42.5.901.

Bartley, J.M., and Wernicke, B.P., 1984, The Snake Range décollement interpreted as a major extensional shear zone: Tectonics, v. 3, p. 647–657, https://doi.org/10.1029/TC003i006p00647.

Behr, W.M., and Platt, J.P., 2011, A naturally constrained stress profile through the middle crust in an extensional terrane: Earth and Planetary Science Letters, v. 303, p. 181–192, https://doi.org/10.1016/j.epsl.2010.11.044.

Behr, W.M., and Platt, J.P., 2014, Brittle faults are weak, yet the ductile middle crust is strong: Implications for lithospheric mechanics: Geophysical Research Letters, v. 41, no. 22, p. 8067–8075, https://doi.org/10.1002/2014GL061349.

Bird, P., 1984, Laramide crustal thickening event in the Rocky Mountain foreland and Great Plains: Tectonics, v. 3, p. 741–758, https://doi.org/10.1029/TC003i007p00741.

Brooks, W.E., Thorman, C.H., and Snee, L.W., 1995, The $^{40}Ar/^{39}Ar$ ages and tectonic setting of the middle Eocene Northeast Nevada volcanic field: Journal of Geophysical Research–Solid Earth, v. 100, p. 10,403–10,416, https://doi.org/10.1029/94JB03389.

Brueseke, M.E., Callicoat, J.S., Hames, W., and Larson, P.B., 2014, Mid-Miocene rhyolite volcanism in northeastern Nevada: The Jarbidge Rhyolite and its relationship to the Cenozoic evolution of the northern Great Basin (USA): Geological Society of America Bulletin, v. 126, p. 1047–1067, https://doi.org/10.1130/B30736.1.

Buck, W.R., 1988, Flexural rotation of normal faults: Tectonics, v. 7, p. 959–973, https://doi.org/10.1029/TC007i005p00959.

Byerlee, J., 1978, Friction of rocks, *in* Byerlee, D., and Wyss, M., eds., Rock Friction and Earthquake Prediction: Basel, Switzerland, Birkhäuser, p. 615–626, https://doi.org/10.1007/978-3-0348-7182-2_4.

Bykerk-Kauffman, A., and Janecke, S.U., 1987, Late Cretaceous to early Tertiary ductile deformation: Catalina-Rincon metamorphic core complex, southeastern Arizona: Geology, v. 15, p. 462–465, https://doi.org/10.1130/0091-7613(1987)15<462:LCTETD>2.0.CO;2.

Camilleri, P., 2010a, Geologic Map of the Northern Pequop Mountains, Elko County, Nevada: Nevada Bureau of Mines and Geology Map 171, scale 1:48,000.

Camilleri, P., 2010b, Geologic Map of the Wood Hills, Elko County, Nevada: Nevada Bureau of Mines and Geology Map 172, scale 1:48,000.

Camilleri, P.A., and Chamberlain, K.R., 1997, Mesozoic tectonics and metamorphism in the Pequop Mountains and Wood Hills region, northeast Nevada: Implications for the architecture and evolution of the Sevier orogen: Geological Society of America Bulletin, v. 109, p. 74–94, https://doi.org/10.1130/0016-7606(1997)109<0074:MTAMIT>2.3.CO;2.

Camilleri, P., Deibert, J., and Perkins, M., 2017, Middle Miocene to Holocene tectonics, basin evolution, and paleogeography along the southern margin of the Snake River Plain in the Knoll Mountain–Ruby–East Humboldt Range region, northeastern Nevada and south-central Idaho: Geosphere, v. 13, p. 1901–1948, https://doi.org/10.1130/GES01318.1.

Canada, A.S., Cassel, E.J., McGrew, A.J., Smith, M.E., Stockli, D.F., Foland, K.A., Jicha, B., and Singer, B.S., 2019, Eocene exhumation and extensional basin formation in the Copper Mountains, Nevada, USA: Geosphere, v. 15, p. 1577–1597, https://doi.org/10.1130/GES02101.1.

Chapman, J.B., Ducea, M.N., DeCelles, P.G., and Profeta, L., 2015, Tracking changes in crustal thickness during orogenic evolution with Sr/Y: An example from the North American Cordillera: Geology, v. 43, p. 919–922, https://doi.org/10.1130/G36996.1.

Chapman, J.B., Runyon, S.E., Shields, J., Lawler, B.L., Pridmore, C.J., Scoggin, S.H., Swaim, N.T., Trzinski, A.E., Wiley, H.N., Barth, A.P., and Haxel, G.B., 2021, The North American Cordilleran anatectic belt: Earth-Science Reviews, v. 215, https://doi.org/10.1016/j.earscirev.2021.103576.

Clennett, E.J., Sigloch, K., Mihalynuk, M.G., Seton, M., Henderson, M.A., Hosseini, K., Mohammadzaheri, A., Johnston, S.T., and Müller, R.D., 2020, A quantitative tomotectonic plate reconstruction of western North America and the eastern Pacific basin: Geochemistry, Geophysics, Geosystems, v. 21, https://doi.org/10.1029/2020GC009117.

Coats, R.R., 1987, Geologic Map of Elko County, Nevada: Nevada Bureau of Mines and Geology Bulletin 101, scale 1:250,000.

Colgan, J.P., and Henry, C.D., 2009, Rapid middle Miocene collapse of the Mesozoic orogenic plateau in north-central Nevada: International Geology Review, v. 51, p. 920–961, https://doi.org/10.1080/00206810903056731.

Colgan, J.P., Howard, K.A., Fleck, R.J., and Wooden, J.L., 2010, Rapid middle Miocene extension and unroofing of the southern Ruby Mountains, Nevada: Tectonics, v. 29, TC6022, https://doi.org/10.1029/2009TC002655.

Colgan, J.P., Johnstone, S.A., and Shuster, D.L., 2020, Timing of Cenozoic extension in the southern Stillwater Range and Dixie Valley, Nevada: Tectonics, v. 39, https://doi.org/10.1029/2019TC005757.

Collettini, C., 2011, The mechanical paradox of low-angle normal faults: Current understanding and open questions: Tectonophysics, v. 510, p. 253–268, https://doi.org/10.1016/j.tecto.2011.07.015.

Collettini, C., and Sibson, R.H., 2001, Normal faults, normal friction?: Geology, v. 29, p. 927–930, https://doi.org/10.1130/0091-7613(2001)029<0927:NFNF>2.0.CO;2.

Coney, P.J., 1974, Structural analysis of the Snake Range "décollement," east-central Nevada: Geological Society of America Bulletin, v. 85, p. 973–978, https://doi.org/10.1130/0016-7606(1974)85<973:SAOTSR>2.0.CO;2.

Coney, P.J., 1980, Cordilleran metamorphic core complexes: An overview, *in* Crittenden, M.D., Jr., Coney, P.J., and Davis, G.H., eds., Cordilleran Metamorphic Core Complexes: Geological Society of America Memoir 153, p. 7–31, https://doi.org/10.1130/MEM153-p7.

Copeland, P., Currie, C.A., Lawton, T.F., and Murphy, M.A., 2017, Location, location, location: The variable lifespan of the Laramide orogeny: Geology, v. 45, p. 223–226, https://doi.org/10.1130/G38810.1.

Crittenden, M.D., Jr., Coney, P.J., and Davis, G.H., eds., 1980, Cordilleran Metamorphic Core Complexes: Geological Society of America Memoir 153, 490 p., https://doi.org/10.1130/MEM153-p485.

Dallmeyer, R.D., Snoke, A.W., and McKee, E.H., 1986, The Mesozoic–Cenozoic tectonothermal evolution of the Ruby Mountains, East Humboldt Range, Nevada: A Cordilleran metamorphic core complex: Tectonics, v. 5, p. 931–954, https://doi.org/10.1029/TC005i006p00931.

Davis, G.A., 1988, Rapid upward transport of mid-crustal mylonitic gneisses in the footwall of a Miocene detachment fault, Whipple Mountains, southeastern California: Geologische Rundschau, v. 77, no. 1, p. 191–209, https://doi.org/10.1007/BF01848684.

Davis, G.A., Lister, G.S., and Reynolds, S.J., 1986, Structural evolution of the Whipple and South Mountains shear zones, southwestern United States: Geology, v. 14, p. 7–10, https://doi.org/10.1130/0091-7613(1986)14<7:SEOTWA>2.0.CO;2.

Davis, G.H., 2013, Localization control for chlorite breccia deformation beneath Catalina detachment fault, Rincon Mountains, Tucson, Arizona: Journal of Structural Geology, v. 50, p. 237–253, https://doi.org/10.1016/j.jsg.2012.12.001.

DeCelles, P.G., 2004, Late Jurassic to Eocene evolution of the Cordilleran thrust belt and foreland basin system, western USA: American Journal of Science, v. 304, p. 105–168, https://doi.org/10.2475/ajs.304.2.105.

Dee, S., Dering, G., and Henry, C., 2015, Preliminary Geologic Map of the Heelfly Creek Quadrangle and Adjacent Parts of the Tent Mountain, Soldier Peak, and Secret Valley Quadrangles, Elko County, Nevada: Nevada Bureau of Mines and Geology Open-File Report 15-4, scale 1:24,000.

Dokka, R.K., Mahaffie, M.J., and Snoke, A.W., 1986, Thermochronologic evidence of major tectonic denudation associated with detachment faulting, northern Ruby Mountains–East Humboldt Range, Nevada: Tectonics, v. 5, p. 995–1006, https://doi.org/10.1029/TC005i007p00995.

Ducea, M.N., Triantafyllou, A., and Krcmaric, J., 2020, New timing and depth constraints for the Catalina metamorphic core complex, southeast Arizona: Tectonics, v. 39, https://doi.org/10.1029/2020TC006383.

Egger, A.E., Dumitru, T.A., Miller, E.L., Savage, C.F., and Wooden, J.L., 2003, Timing and nature of Tertiary plutonism and extension in the Grouse Creek Mountains, Utah: International Geology Review, v. 45, p. 497–532, https://doi.org/10.2747/0020-6814.45.6.497.

Gans, P.B., and Gentry, B.J., 2016, Dike emplacement, footwall rotation, and the transition from magmatic to tectonic extension in the Whipple Mountains metamorphic core complex, southeastern California: Tectonics, v. 35, p. 2564–2608, https://doi.org/10.1002/2016TC004215.

Gans, P.B., Seedorff, E., Fahey, P.L., Hasler, R.W., Maher, D.J., Jeanne, R.A., and Shaver, S.A., 2001, Rapid Eocene extension in the Robinson district, White Pine County, Nevada: Constraints from $^{40}Ar/^{39}Ar$ dating: Geology, v. 29, p. 475–478, https://doi.org/10.1130/0091-7613(2001)029<0475:REEITR>2.0.CO;2.

Gifford, J.N., Foster, D.A., Howard, K.A., Newman, V., and Donelick, R., 2008, Quantifying Eocene and Miocene extension in the Ruby–East Humboldt metamorphic core complex, northeastern Nevada, *in* Garver, J.I., and Montario, M.J., eds., Proceedings from the 11th International Conference on Thermochronometry: Anchorage, Alaska, September 2008.

Gilbert, H., 2012, Crustal structure and signatures of recent tectonism as influenced by ancient terranes in the western United States: Geosphere, v. 8, no. 1, p. 141–157, https://doi.org/10.1130/GES00720.1.

Gold, R.D., Stephenson, W.J., Briggs, R.W., DuRoss, C.B., Kirby, E., Woolery, E., Delano, J., and Odum, J.K., 2020, Seismic reflection imaging of the low-angle Panamint normal fault system, eastern California: Journal of Geophysical Research: Solid Earth, v. 125, https://doi.org/10.1029/2020JB020243.

Gottardi, R., McAleer, R., Casale, G., Borel, M., Iriondo, A., and Jepson, G., 2020, Exhumation of the Coyote Mountains metamorphic core complex (Arizona): Implications for orogenic collapse of the southern North American Cordillera: Tectonics, v. 39, no. 8, https://doi.org/10.1029/2019TC006050.

Haines, S.H., and van der Pluijm, B.A., 2010, Dating the detachment fault system of the Ruby Mountains, Nevada: Significance for the kinematics of low-angle normal faults: Tectonics, v. 29, https://doi.org/10.1029/2009TC002552.

Hallett, B.W., and Spear, F.S., 2014, The *P-T* history of anatectic pelites of the northern East Humboldt Range, Nevada: Evidence for tectonic loading, decompression, and anatexis: Journal of Petrology, v. 55, p. 3–36, https://doi.org/10.1093/petrology/egt057.

Hallett, B.W., and Spear, F.S., 2015, Versatile monazite: Resolving geological records and solving challenges in materials science. Monazite, zircon, and garnet growth in migmatitic pelites as a record of metamorphism and partial melting in the East Humboldt Range, Nevada: The American Mineralogist, v. 100, p. 951–972, https://doi.org/10.2138/am-2015-4839.

Harrison, T.M., Duncan, I.A.N., and Mcdougall, I.A.N., 1985, Diffusion of ^{40}Ar in biotite: Temperature, pressure and compositional effects: Geochimica et Cosmochimica Acta, v. 49, p. 2461–2468, https://doi.org/10.1016/0016-7037(85)90246-7.

Haynes, S.R., 2003, Development of the Eocene Elko Basin, Northeastern Nevada: Implications for Paleogeography and Regional Tectonism [M.S. thesis]: Vancouver, British Columbia, University of British Columbia, 159 p.

Henry, C.D., 2008, Ash-flow tuffs and paleovalleys in northeastern Nevada: Implications for Eocene paleogeography and extension in the Sevier hinterland, northern Great Basin: Geosphere, v. 4, p. 1–35, https://doi.org/10.1130/GES00122.1.

Henry, C.D., 2018, The Eocene Elko Basin and Elko Formation, NE Nevada: Paleotopographic Controls on Area, Thickness, Facies Distribution, and Petroleum Potential: American Association of Petroleum Geologists Search and Discovery article 11102.

Henry, C.D., McGrew, A.J., Colgan, J.P., Snoke, A.W., and Brueseke, M.E., 2011, Timing, distribution, amount, and style of Cenozoic extension in the northern Great Basin, *in* Lee, J., and Evans, J.P., eds., Geologic Field Trips to the Basin and Range, Rocky Mountains, Snake River Plain, and Terranes of the U.S. Cordillera: Geological Society of America Field Guide 21, p. 27–66, https://doi.org/10.1130/2011.0021(02).

Henry, C.D., Hinz, N.H., Faulds, J.E., Colgan, J.P., John, D.A., Brooks, E.R., Cassel, E.J., Garside, L.J., Davis, D.A., and Castor, S.B., 2012, Eocene–early Miocene paleotopography of the Sierra Nevada–Great Basin–Nevadaplano based on widespread ash-flow tuffs and paleovalleys: Geosphere, v. 8, p. 1–27, https://doi.org/10.1130/GES00727.1.

Howard, K.A., 1966, Structure of the Metamorphic Rocks of the Northern Ruby Mountains, Nevada [Ph.D. thesis]: New Haven, Connecticut, Yale University, 170 p.

Howard, K.A., 1971, Paleozoic metasediments in the northern Ruby Mountains, Nevada: Geological Society of America Bulletin, v. 82, p. 259–264, https://doi.org/10.1130/0016-7606(1971)82[259:PMITNR]2.0.CO;2.

Howard, K.A., 1980, Metamorphic infrastructure in the northern Ruby Mountains, Nevada, *in* Crittenden, M.D., Jr., Coney, P.J., and Davis, G.H., eds., Cordilleran Metamorphic Core Complexes: Geological Society of America Memoir 153, p. 335–348, https://doi.org/10.1130/MEM153-p335.

Howard, K.A., Kistler, R.W., Snoke, A.W., and Willden, R., 1979, Geologic map of the Ruby Mountains, Nevada: U.S. Geological Survey Map I-1136, scale 1:125,000.

Howard, K.A., Wooden, J.L., Barnes, C.G., Premo, W.R., Snoke, A.W., and Lee, S.Y., 2011, Episodic growth of a Late Cretaceous and Paleogene intrusive complex of pegmatitic leucogranite, Ruby Mountains core complex, Nevada, USA: Geosphere, v. 7, p. 1220–1248, https://doi.org/10.1130/GES00668.1.

Howlett, C.J., Reynolds, A.N., and Laskowski, A.K., 2021, Magmatism and extension in the Anaconda metamorphic core complex of western Montana and relation to regional tectonics: Tectonics, v. 40, no. 9, https://doi.org/10.1029/2020TC006431.

Hudec, M.R., 1992, Mesozoic structural and metamorphic history of the central Ruby Mountains metamorphic core complex, Nevada: Geological Society of America Bulletin, v. 104, no. 9, p. 1086–1100, https://doi.org/10.1130/0016-7606(1992)104<1086:MSAMHO>2.3.CO;2.

Hurlow, H.A., 1987, Structural Geometry, Fabric, and Chronology of a Tertiary Extensional Shear Zone–Detachment System [M.S. thesis]: Laramie, Wyoming, University of Wyoming, 140 p.

Hurlow, H.A., Snoke, A.W., and Hodges, K.V., 1991, Temperature and pressure of mylonitization in a Tertiary extensional shear zone, Ruby Mountains–East Humboldt Range, Nevada: Tectonic implications: Geology, v. 19, p. 82–86, https://doi.org/10.1130/0091-7613(1991)019<0082:TAPOMI>2.3.CO;2.

Jaramillo, V., Catlos, E., Bell, E., Stockli, D.F., Schmitt, A.K., Chin, E.J., and Yin, A., 2022, Superposition of 80–55 Ma high *P-T* (0.7 GPa/750 °C) metamorphism by mid-Tertiary detachment faulting in the Whipple Mountains, SE California: Geological Society of America Abstracts with Programs, v. 54, no. 5, https://doi.org/10.1130/abs/2022AM-378171.

Jones, C.H., Sonder, L.J., and Unruh, J.R., 1998, Lithospheric gravitational potential energy and past orogenesis: Implications for conditions of initial Basin and Range and Laramide deformation: Geology, v. 26, no. 7, p. 639–642, https://doi.org/10.1130/0091-7613(1998)026<0639:LGPEAP>2.3.CO;2.

Jones, J.V., 1999, Deformational, Magmatic, and Metamorphic History of the Central Ruby Mountains, Elko County, Nevada [M.S. thesis]: Laramie, Wyoming, University of Wyoming, 166 p.

Kapp, P., Taylor, M., Stockli, D., and Ding, L., 2008, Development of active low-angle normal fault systems during orogenic collapse: Insight from Tibet: Geology, v. 36, p. 7–10, https://doi.org/10.1130/G24054A.1.

Kohli, A.H., and Zoback, M.D., 2013, Frictional properties of shale reservoir rocks: Journal of Geophysical Research: Solid Earth, v. 118, p. 5109–5125, https://doi.org/10.1002/jgrb.50346.

Konstantinou, A., Strickland, A., Miller, E.L., and Wooden, J.P., 2012, Multistage Cenozoic extension of the Albion–Raft River–Grouse Creek metamorphic core complex: Geochronologic and stratigraphic constraints: Geosphere, v. 8, p. 1429–1466, https://doi.org/10.1130/GES00778.1.

Konstantinou, A., Strickland, A., Miller, E., Vervoort, J., Fisher, C.M., Wooden, J., and Valley, J., 2013, Synextensional magmatism leading to crustal flow in the Albion–Raft River–Grouse Creek metamorphic core complex, northeastern Basin and Range: Tectonics, v. 32, p. 1384–1403, https://doi.org/10.1002/tect.20085.

Kruckenberg, S.C., Whitney, D.L., Teyssier, C., Fanning, C.M., and Dunlap, W.J., 2008, Paleocene–Eocene migmatite crystallization, extension, and exhumation in the hinterland of the northern Cordillera: Okanogan dome, Washington, USA: Geological Society of America Bulletin, v. 120, p. 912–929, https://doi.org/10.1130/B26153.1.

Kruckenberg, S.C., Vanderhaeghe, O., Ferré, E.C., Teyssier, C., and Whitney, D.L., 2011, Flow of partially molten crust and the internal dynamics of a migmatite dome, Naxos, Greece: Tectonics, v. 30, no. 3, TC3001, https://doi.org/10.1029/2010TC002751.

Lee, J., Blackburn, T., and Johnston, S., 2017, Timing of mid-crustal ductile extension in the northern Snake Range metamorphic core complex, Nevada: Evidence from U/Pb zircon ages: Geosphere, v. 13, p. 439–459, https://doi.org/10.1130/GES01429.1.

Lee, S.Y., Barnes, C.G., Snoke, A.W., Howard, K.A., and Frost, C.D., 2003, Petrogenesis of Mesozoic, peraluminous granites in the Lamoille Canyon area, Ruby Mountains, Nevada, USA: Journal of Petrology, v. 44, no. 4, p. 713–732, https://doi.org/10.1093/petrology/44.4.713.

Levy, D. A., Zuza, A. V., Michels, Z. D., and DesOrmeau, J. W., 2023, Buoyant doming generates metamorphic core complexes in the North American Cordillera: Geology, v. 51, no. 3, p. 290–294, https://doi.org/10.1130/G50752.1.

Lister, G.S., and Davis, G.A., 1989, The origin of metamorphic core complexes and detachment faults formed during Tertiary continental extension in the northern Colorado River region, USA: Journal of Structural Geology, v. 11, p. 65–94, https://doi.org/10.1016/0191-8141(89)90036-9.

Lund Snee, J.E., Miller, E.L., Grove, M., Hourigan, J.K., and Konstantinou, A., 2016, Cenozoic paleogeographic evolution of the Elko Basin and surrounding region, northeast Nevada: Geosphere, v. 12, p. 464–500, https://doi.org/10.1130/GES01198.1.

Lush, A.P., McGrew, A.J., Snoke, A.W., and Wright, J.E., 1988, Allochthonous Archean basement in the northern East Humboldt Range, Nevada: Geology, v. 16, no. 4, p. 349–353, https://doi.org/10.1130/0091-7613(1988)016<0349:AABITN>2.3.CO;2.

MacCready, T., Snoke, A.W., Wright, J.E., and Howard, K.A., 1997, Mid-crustal flow during Tertiary extension in the Ruby Mountains core complex, Nevada: Geological Society of America Bulletin, v. 109, p. 1576–1594, https://doi.org/10.1130/0016-7606(1997)109%3C1576:MCFDTE%3E2.3.CO;2.

McGrew, A.J., 2018, Geologic Map of the Humboldt Peak Quadrangle, Elko County, Nevada: Nevada Bureau of Mines Map 186, scale 1:24,000, 23 p.

McGrew, A.J., and Snee, L.W., 1994, ^{40}Ar/^{39}Ar thermochronologic constraints on the tectonothermal evolution of the northern East Humboldt Range metamorphic core complex, Nevada: Tectonophysics, v. 238, p. 425–450, https://doi.org/10.1016/0040-1951(94)90067-1.

McGrew, A.J., and Snoke, A.W., 2015, Geologic Map of the Welcome Quadrangle and an Adjacent Part of the Wells Quadrangle, Elko County, Nevada: Nevada Bureau of Mines and Geology Map 184, scale 1:24,000, 40 p.

McGrew, A.J., Peters, M.T., and Wright, J.E., 2000, Thermobarometric constraints on the tectonothermal evolution of the East Humboldt Range metamorphic core complex, Nevada: Geological Society of America Bulletin, v. 112, p. 45–60, https://doi.org/10.1130/0016-7606(2000)112<45:TCOTTE>2.0.CO;2.

Miller, C.F., and Bradfish, L.J., 1980, An inner Cordilleran belt of muscovite-bearing plutons: Geology, v. 8, p. 412–416, https://doi.org/10.1130/0091-7613(1980)8<412:AICBOM>2.0.CO;2.

Miller, E.L., Gans, P.B., and Garing, J., 1983, The Snake Range décollement: An exhumed mid-Tertiary ductile-brittle transition: Tectonics, v. 2, p. 239–263, https://doi.org/10.1029/TC002i003p00239.

Miller, E.L., Dumitru, T.A., Brown, R.W., and Gans, P.B., 1999, Rapid Miocene slip on the Snake Range–Deep Creek range

fault system, east-central Nevada: Geological Society of America Bulletin, v. 111, p. 886–905, https://doi.org/10.1130/0016-7606(1999)111<0886:RMSOTS>2.3.CO;2.

Numelin, T., Marone, C., and Kirby, E., 2007, Frictional properties of natural fault gouge from a low-angle normal fault, Panamint Valley, California: Tectonics, v. 26, TC2004, https://doi.org/10.1029/2005TC001916.

Platt, J.P., Behr, W.M., and Cooper, F.J., 2015, Metamorphic core complexes: Windows into the mechanics and rheology of the crust: Journal of the Geological Society, v. 172, p. 9–27, https://doi.org/10.1144/jgs2014-036.

Pollard, D.D., and Segall, P., 1987, Theoretical displacements and stresses near fractures in rock: With applications to faults, joints, veins, dikes, and solution surfaces, *in* Atkinson, B.K., ed., Fracture Mechanics of Rock: London, Academic Press, p. 277–349, https://doi.org/10.1016/B978-0-12-066266-1.50013-2.

Ponce, D.A., Watt, J.T., and Bouligand, C., 2011, Geophysical Setting of the 21 February 2008 Mw 6.0 Wells Earthquake, Nevada, and Implications for Earthquake Hazards: Nevada Bureau of Mines and Geology Special Publication 36, 12 p.

Premo, W.R., Castiñeiras, P., and Wooden, J.L., 2008, SHRIMP-RG U-Pb isotopic systematics of zircon from the Angel Lake orthogneiss, East Humboldt Range, Nevada: Is this really Archean crust?: Geosphere, v. 4, p. 963–975, https://doi.org/10.1130/GES00164.1.

Satarugsa, P., and Johnson, R.A., 2000, Cenozoic tectonic evolution of the Ruby Mountains metamorphic core complex and adjacent valleys, northeastern Nevada: Rocky Mountain Geology, v. 35, p. 205–230, https://doi.org/10.2113/35.2.205.

Say, M.C., and Zuza, A.V., 2021, Heterogenous late Miocene extension in the northern Walker Lane (California-Nevada, USA) demonstrates vertically decoupled crustal extension: Geosphere, v. 17, p. 1762–1785, https://doi.org/10.1130/GES02409.1.

Schellart, W.P., Stegman, D.R., Farrington, R.J., Freeman, J., and Moresi, L., 2010, Cenozoic tectonics of western North America controlled by evolving width of Farallon slab: Science, v. 329, p. 316–319, https://doi.org/10.1126/science.1190366.

Sharp, R.P., 1939, The Miocene Humboldt Formation in northeastern Nevada: The Journal of Geology, v. 47, p. 133–160, https://doi.org/10.1086/624749.

Sicard, K.R., and Snoke, A.W., 2020, Geologic Map of the Gordon Creek Quadrangle, Elko County, Nevada: Nevada Bureau of Mines and Geology Map 188, scale 1:24,000, 28 p.

Singleton, J.S., and Mosher, S., 2012, Mylonitization in the lower plate of the Buckskin-Rawhide detachment fault, west-central Arizona: Implications for the geometric evolution of metamorphic core complexes: Journal of Structural Geology, v. 39, p. 180–198, https://doi.org/10.1016/j.jsg.2012.02.013.

Smith, J.F., and Ketner, K.B., 1978, Geologic Map of the Carlin–Pinon Range Area, Elko and Eureka Counties, Nevada: U.S. Geological Survey Miscellaneous Investigations Map 1028, scale 1:62,500, https://doi.org/10.3133/i1028.

Smith, M.E., Cassel, E.J., Jicha, B.R., Singer, B.S., and Canada, A.S., 2017, Hinterland drainage closure and lake formation in response to middle Eocene Farallon slab removal, Nevada, USA: Earth and Planetary Science Letters, v. 479, p. 156–169, https://doi.org/10.1016/j.epsl.2017.09.023.

Snelson, S., 1957, The geology of the northern Ruby Mountains and eastern Humboldt Range, Elko County, northeastern Nevada [Ph.D. dissertation]: Seattle, Washington, University of Washington, 268 p.

Snoke, A.W., 1980, Transition from infrastructure to suprastructure in the northern Ruby Mountains, Nevada, *in* Crittenden, M.D., Jr., Coney, P.J., and Davis, G.H., eds., Cordilleran Metamorphic Core Complexes: Geological Society of America Memoir 153, p. 287–334, https://doi.org/10.1130/MEM153-p287.

Snoke, A.W., and Miller, D.M., 1988, Metamorphic and tectonic history of the northeastern Great Basin, *in* Ernst, W.G., ed., Metamorphic and Tectonic Evolution of the Western United States: Englewood Cliffs, New Jersey, Prentice-Hall, p. 606–648.

Snoke, A.W., McGrew, A.J., Valasek, P.A., and Smithson, S.B., 1990, A crustal cross-section for a terrain of superimposed shortening and extension: Ruby Mountains–East Humboldt Range metamorphic core complex, Nevada, *in* Salisbury, M.H., and Fountain, D.M., eds., Exposed Cross-Sections of the Continental Crust: Dordrecht, Netherlands, Springer, p. 103–135, https://doi.org/10.1007/978-94-009-0675-4_5.

Snoke, A.W., Howard, K.A., McGrew, A.J., Burton, B.R., Barnes, C.G., Peters, M.T., and Wright, J.E., 1997, The grand tour of the Ruby–East Humboldt metamorphic core complex, northeastern Nevada: Part 1—Introduction & road log: Brigham Young University Geology Studies, v. 42, p. 225–296.

Snoke, A.W., Howard, K., and Dee, S., 2021, Geologic Map of the Secret Valley Quadrangle, Elko County, Nevada: Nevada Bureau of Mines and Geology Map 189, scale 1:24,000.

Snoke, A.W., Howard, K., and Dee, S., 2022, Geologic Map of the Soldier Peak Quadrangle, Elko County, Nevada: Nevada Bureau of Mines and Geology Map 191, scale 1:24,000.

Solomon, B.J., McKee, E.H., and Andersen, D.W., 1979, Stratigraphy and depositional environments of Paleogene rocks near Elko, Nevada, *in* Armentrout, J.M., Cole, M.R., and Ter-Best, H., Jr., eds., Cenozoic Paleogeography of the Western United States: Anaheim, California, Pacific Section, Society of Economic Paleontologists and Mineralogists, Pacific Coast Paleogeography Symposium 3, p. 75–88.

Sonder, L.J., and Jones, C.H., 1999, Western United States extension: How the west was widened: Annual Review of Earth and Planetary Sciences, v. 27, no. 1, p. 417–462, https://doi.org/10.1146/annurev.earth.27.1.417.

Spencer, J.E., 1982, Origin of folds of Tertiary low-angle fault surfaces, southeastern California and western Arizona, *in* Frost, E.G., and Martin, D.L., eds., Mesozoic–Cenozoic Tectonic Evolution of the Colorado River Region, California, Nevada and Arizona: San Diego, California, Cordilleran Publishers, p. 123–134.

Spencer, J.E., 1985, Miocene low-angle normal faulting and dike emplacement, Homer Mountain and surrounding areas, southeastern California and southernmost Nevada: Geological Society of America Bulletin, v. 96, p. 1140–1155, https://doi.org/10.1130/0016-7606(1985)96<1140:MLNFAD>2.0.CO;2.

Spencer, J.E., and Reynolds, S.J., 1989, Middle Tertiary tectonics of Arizona and adjacent areas, *in* Jenney, J.P., and Reynolds, S.J., eds., Geologic Evolution of Arizona: Arizona Geological Society Digest, v. 17, p. 539–574.

Spencer, J.E., Richard, S.M., Bykerk-Kauffman, A., Constenius, K.N., and Valencia, V.A., 2022, Structure, chronology, kinematics, and geodynamics of tectonic extension in the greater Catalina metamorphic core complex, southeastern Arizona, USA: Geosphere, v. 18, p. 1643–1678, https://doi.org/10.1130/GES02485.1.

Stewart, J.H., 1980, Regional tilt patterns of late Cenozoic basin-range fault blocks, western United States: Geological Society of America Bulletin, v. 91, no. 8, p. 460–464, https://doi.org/10.1130/0016-7606(1980)91%3C460:RTPOLC%3E2.0.CO;2.

Strickland, A., Miller, E.L., and Wooden, J.L., 2011a, The timing of Tertiary metamorphism and deformation in the Albion–Raft River–Grouse Creek metamorphic core complex, Utah and Idaho: The Journal of Geology, v. 119, p. 185–206, https://doi.org/10.1086/658294.

Strickland, A., Miller, E.L., Wooden, J.L., Kozdon, R., and Valley, J.W., 2011b, Syn-extensional plutonism and peak metamorphism in the Albion–Raft River–Grouse Creek metamorphic core complex: American Journal of Science, v. 311, p. 261–314, https://doi.org/10.2475/04.2011.01.

Strickland, A., 2010, Polyphase Deformation and Metamorphism: A Geochronologic Perspective [Ph.D. dissertation]: Stanford, California, Stanford University, 257 p.

Taylor, G.K., 1984, Stratigraphy, Metamorphism, and Structure of the Southeastern East Humboldt Range, Elko County, Nevada [M.S. thesis]: Columbia, South Carolina, University of South Carolina, 148 p.

Thorman, C.H., 1962, Structure and Stratigraphy of the Wood Hills and a Portion of the Northern Pequop Mountains, Elko County, Nevada [Ph.D. dissertation]: Seattle, Washington, University of Washington, 218 p.

Turcotte, D.L., and Schubert, G., 2002, Geodynamics: Cambridge, UK, Cambridge University Press, 636 p., https://doi.org/10.1017/CBO9780511807442.

Wallace, A.R., Perkins, M.E., and Fleck, R.J., 2008, Late Cenozoic paleogeographic evolution of northeastern Nevada: Evidence from the sedimentary basins: Geosphere, v. 4, p. 36–74, https://doi.org/10.1130/GES00114.1.

Wernicke, B., 1995, Low-angle normal faults and seismicity: A review: Journal of Geophysical Research: Solid Earth, v. 100, no. B10, p. 20,159–20,174, https://doi.org/10.1029/95JB01911.

Wernicke, B., and Axen, G.J., 1988, On the role of isostasy in the evolution of normal fault systems: Geology, v. 16, p. 848–851, https://doi.org/10.1130/0091-7613(1988)016<0848:OTROII>2.3.CO;2.

Wernicke, B., Burchfiel, B.C., Lipman, P.W., and Zoback, M.L., 1992, Cenozoic extensional tectonics of the US Cordillera, *in* Burchfiel, B.C., Lipman, B.C., and Zoback, M.L., eds., The Cordilleran Orogen: Conterminous U.S.: Boulder, Colorado, The Geological Society of America, The Geology of North America, v. G-3, p. 553–581, https://doi.org/10.1130/DNAG-GNA-G3.553.

Wesnousky, S.G., and Willoughby, C.H., 2003, Neotectonic note: The Ruby–East Humboldt Range, northeastern Nevada: Bulletin of the Seismological Society of America, v. 93, no. 3, p. 1345–1354, https://doi.org/10.1785/0120020032.

Whitney, D.L., Teyssier, C., Rey, P., and Buck, W.R., 2013, Continental and oceanic core complexes: Geological Society of America Bulletin, v. 125, p. 273–298, https://doi.org/10.1130/B30754.1.

Wong, M.S., and Gans, P.B., 2008, Geologic, structural, and thermochronologic constraints on the tectonic evolution of the Sierra Mazatán core complex, Sonora, Mexico: New insights into metamorphic core complex formation: Tectonics, v. 27, TC4013, https://doi.org/10.1029/2007TC002173.

Wong, M.S., Singleton, J.S., Seymour, N.M., Gans, P.B., and Wrobel, A.J., 2023, Late Cretaceous–early Paleogene extensional

ancestry of the Harcuvar and Buckskin-Rawhide metamorphic core complexes, western Arizona: Tectonics, v. 42, no. 2, https://doi.org/10.1029/2022TC007656.

Wright, J.E., and Snoke, A.W., 1993, Tertiary magmatism and mylonitization in the Ruby–East Humboldt metamorphic core complex, northeastern Nevada: U-Pb geochronology and Sr, Nd, and Pb isotope geochemistry: Geological Society of America Bulletin, v. 105, p. 935–952, https://doi.org/10.1130/0016-7606(1993)105<0935:TMAMIT>2.3.CO;2.

Zuza, A.V., and Cao, W., 2023, Metamorphic core complex dichotomy in the North American Cordillera explained by buoyant upwelling in variably thick crust: GSA Today, v. 33, no. 3–4, p. 4–11, https://doi.org/10.1130/GSATG548A.1.

Zuza, A.V., Thorman, C.H., Henry, C.D., Levy, D.A., Dee, S., Long, S.P., Sandberg, C.A., and Soignard, E., 2020, Pulsed Mesozoic deformation in the Cordilleran hinterland and evolution of the Nevadaplano: Insights from the Pequop Mountains, NE Nevada: Lithosphere, v. 2020, https://doi.org/10.2113/2020/8850336.

Zuza, A.V., Dee, S., Hurlow, H.A., Snoke, A.W., and Laabs, B.J.C., 2021a, Geologic Map of the Tent Mountain Quadrangle, Elko County, Nevada: Nevada Bureau of Mines and Geology Open-File Report 2021-03, scale 1:24,000.

Zuza, A.V., Henry, C.D., Dee, S., Thorman, C.H., and Heizler, M.T., 2021b, Records of pulsed intracontinental plateau growth and subsequent collapse in the North American Cordilleran hinterland: Jurassic–Cenozoic tectonics of the Pequop Mountains, NE Nevada: Geosphere, v. 17, p. 2078–2122, https://doi.org/10.1130/GES02307.1.

Zuza, A.V., Levy, D.A., Dee, S., DesOrmeau, J.W., Cheng, F., and Li, X., 2022a, Structural architecture and attenuation of the ductile lower plate of the Ruby Mountain–East Humboldt Range metamorphic core complex, northeast Nevada: Tectonics, v. 41, https://doi.org/10.1029/2021TC007162.

Zuza, A.V., Levy, D.A., and Mulligan, S.R., 2022b, Geologic field evidence for non-lithostatic overpressure recorded in the North American Cordillera hinterland, northeast Nevada: Geoscience Frontiers, v. 13, 101099, https://doi.org/10.1016/j.gsf.2020.10.006.